iScience

CellPress
OPEN ACCESS

Article

Histone H2A ubiquitination resulting from Brap loss of function connects multiple aging hallmarks and accelerates neurodegeneration

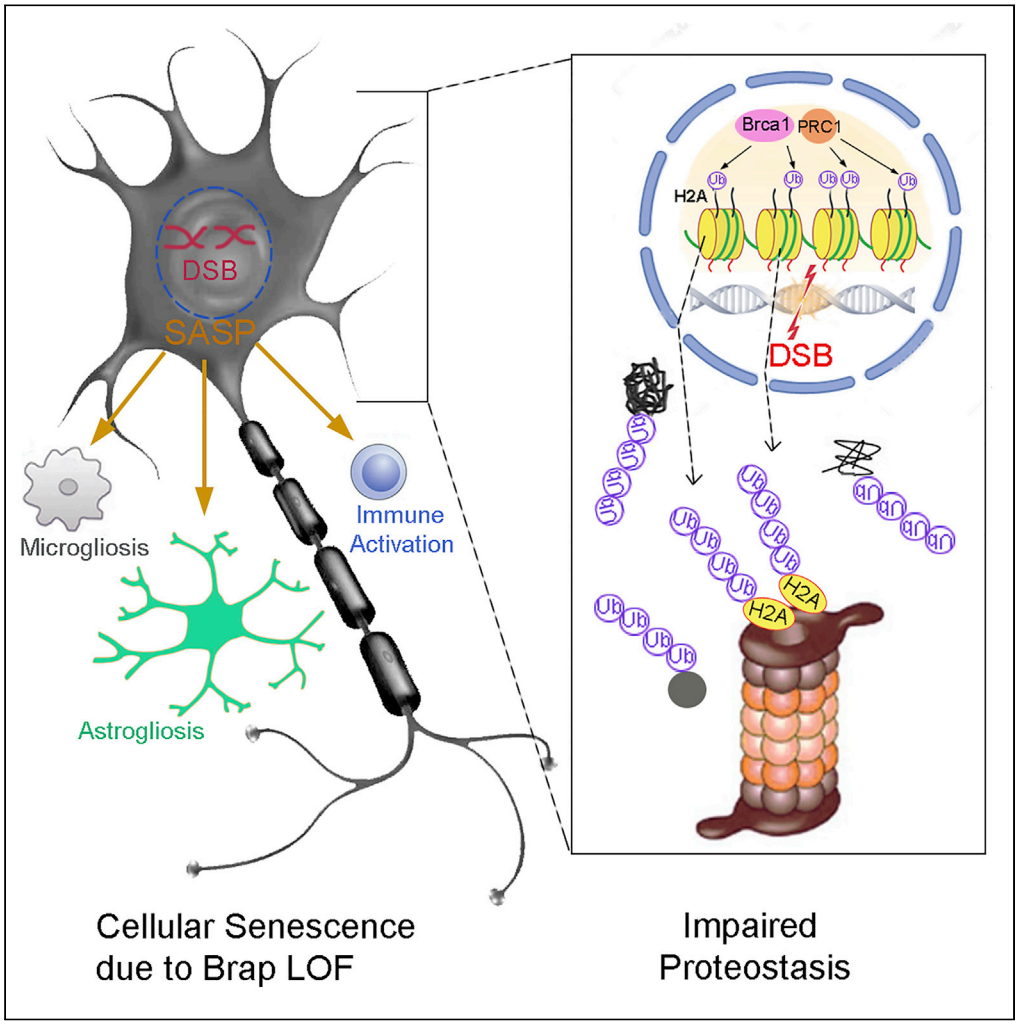

Yan Guo, Alison.A. Chomiak, Ye Hong, ..., Xiaoming Zhou, Edwin S. Monuki, Yuanyi Feng

yuanyi.feng@usuhs.edu

Highlights

Losing BRCA1-associated Brap Results in Sustained DNA Damage and Cellular Senescence

Brap Deficient Cells and Brain Show a Hallmark Increase in Histone H2A Ubiquitination

Transcriptome and Proteome altered by Brap Mediate Neuroinflammation and Proteopathy

Elevated Ubiquityl-H2A is associated with Neurodegeneration and Alzheimer's Disease

Guo et al., iScience 25, 104519
July 15, 2022
https://doi.org/10.1016/j.isci.2022.104519

iScience

CellPress
OPEN ACCESS

Article

Histone H2A ubiquitination resulting from Brap loss of function connects multiple aging hallmarks and accelerates neurodegeneration

Yan Guo,[1,7] Alison.A. Chomiak,[1,8] Ye Hong,[2] Clara C. Lowe,[3,11] Caroline A. Kopsidas,[3] Wen-Ching Chan,[4,9] Jorge Andrade,[4,10] Hongna Pan,[3,12] Xiaoming Zhou,[5] Edwin S. Monuki,[6] and Yuanyi Feng[3,13,*]

SUMMARY

Aging is an intricate process characterized by multiple hallmarks including stem cell exhaustion, genome instability, epigenome alteration, impaired proteostasis, and cellular senescence. Whereas each of these traits is detrimental at the cellular level, it remains unclear how they are interconnected to cause systemic organ deterioration. Here we show that abrogating Brap, a BRCA1-associated protein essential for neurogenesis, results in persistent DNA double-strand breaks and elevation of histone H2A mono- and poly-ubiquitination (H2Aub). These defects extend to cellular senescence and proteasome-mediated histone H2A proteolysis with alterations in cells' proteomic and epigenetic states. Brap deletion in the mouse brain causes neuroinflammation, impaired proteostasis, accelerated neurodegeneration, and substantially shortened the lifespan. We further show the elevation of H2Aub also occurs in human brain tissues with Alzheimer's disease. These data together suggest that chromatin aberrations mediated by H2Aub may act as a nexus of multiple aging hallmarks and promote tissue-wide degeneration.

INTRODUCTION

Aging is a natural process that connects birth and death. The time-dependent decline in organ function during aging is the major risk factor for many diseases including neurodegenerative disorders (NDs). Yet, the etiology of aging is complex and multifactorial. It is associated with multiple cellular and molecular hallmarks, such as stem cell exhaustion, genome instability, epigenetic alteration, deregulated nutrient sensing, mitochondrial dysfunction, cellular senescence, and loss of proteostasis (Lopez-Otin et al., 2013). For neurodegeneration, additional hallmark defects in neuronal calcium homeostasis and neuronetwork activity, as well as increased glial cell activation and neuroinflammation are also essential contributors to the physical and functional deterioration of the brain (Mattson and Arumugam, 2018). Aging at the tissue, organ, and system levels does not simply result from the dysfunction of any individual cellular or molecular process. To cause progressive and irreversible tissue- or organ-wide degeneration, multiple aging promoting factors must act in concert. However, the mechanism underlying the interconnections among various aging hallmarks is poorly understood, forming a major barrier to combating aging-associated diseases.

Among various aging hallmarks, genome instability poses a lifelong threat to all living cells and can result in increased somatic mutations that have been shown to accumulate with age in most organs (Lombard et al., 2005; Soares et al., 2014; White and Vijg, 2016). Besides a clear link to carcinogenesis, a loss of genome stability has also been implicated in neurodegeneration (Bushman et al., 2015; Madabhushi et al., 2014; Mitra et al., 2019; Rulten and Caldecott, 2013; Shanbhag et al., 2019; Thadathil et al., 2019), and there is long-established evidence for significant levels of DNA damage even in non-dividing cells, such as neurons in the brain (Lodato et al., 2015; Lu et al., 2004; Rutten et al., 2007; Suberbielle et al., 2013). Recent whole-genome sequencing analyses have further demonstrated that somatic mutations increase with age in both bulk tissues and single neurons of the human brain (Hoang et al., 2016; Lodato et al., 2018). Moreover, mutations of genes important for genome maintenance and DNA repair cause progeroid syndromes and often manifest with both premature aging and neurodegeneration (Choy and Watters, 2018; Coppede and Migliore, 2010; Kakigi et al., 1992; Weidenheim et al., 2009). Thus, genotoxicity is a universal insult that

[1]Department of Neurology, Northwestern University Feinberg School of Medicine, 303 E. Superior Street, Chicago, IL 60611, USA

[2]University of Turku, Turku 20500, Finland

[3]Department of Biochemistry and Molecular Biology, Uniformed Services University, 4301 Jones Bridge Road, Bethesda, MD 20814, USA

[4]Center for Research Informatics, University of Chicago, Chicago, IL 60637, USA

[5]Department of Medicine, Uniformed Services University, 4301 Jones Bridge Road, Bethesda, MD 20814, USA

[6]Department of Pathology & Laboratory Medicine, University of California, Irvine, CA 92697, USA

[7]Present address: Department of Oncology, Zhengzhou University People's Hospital, Henan Provincial People's Hospital, 7 Weiwu Road, Zhengzhou, Henan, 45003, P.R.C.

[8]Present address: Department of Epigenetics, Van Andel Institute, 333 Bostwick Ave. NE, Grand Rapids, MI 49503, USA

[9]Present address: Natera, 13011A McCallen Pass, Austin, TX 78753, USA

[10]Present address: Kite Pharma, 2400 Broadway, Santa Monica, CA 90404, USA

[11]Present address: Wake Forest University School of Medicine, 475 Vine St, Winston-Salem, NC 27101, USA

[12]Present address: National Institute on Alcohol Abuse and Alcoholism, 5625 Fishers Lane Rockville, MD 20852, USA

Continued

not only is concomitant with old age but also drives aging-associated diseases. Nevertheless, the mechanism by which neuronal DNA damage non-autonomously affects many cells across the brain tissue to promote neurodegeneration remains elusive.

A plausible mechanism for DNA damage to induce tissue-wide degeneration is via cellular senescence, a stress response that occurs when cells experience telomere erosion, chronic oncogenic stimulation, persistent DNA damage, oxidative and metabolic stresses, or mitochondrial dysfunction (Hayflick, 1965; Hernandez-Segura et al., 2018; McHugh and Gil, 2018; Munoz-Espin and Serrano, 2014; Rodier and Campisi, 2011). Although originally defined by a permanent replication arrest, cellular senescence is also characterized by a set of distinctive phenotypes, including the activation of senescence-associated β-galactosidase (SA-β-gal), expression of a cyclin-dependent kinase inhibitor (CKI) $p16^{Ink4a}$, alterations of global epigenetic and metabolic profiles, resistance to apoptosis, increases in autophagy, and implementation of a complex and multicomponent secretome known as the senescence-associated secretory phenotypes (SASP) (Campisi and Robert, 2014; Coppe et al., 2008; Munoz-Espin and Serrano, 2014; Rodier and Campisi, 2011). Through SASP, senescent cells produce a myriad of pro-inflammatory cytokines, chemokines, growth factors, and proteases (Kuilman and Peeper, 2009; Lasry and Ben-Neriah, 2015). These secreted molecules act through autocrine and paracrine signaling to not only reinforce the senescence state, but also non-autonomously affect neighboring cells in the tissue. Remarkably, senescence-like phenotypes have also been observed in neurons with tau aggregation and neurofibrillary tangles of the Alzheimer's disease (AD) brains (Musi et al., 2018). Therefore, it is possible that neurons, which are replication-incompetent by nature, can acquire the additional characteristics of senescent cells upon chronic DNA damage to promote neuroinflammation and neurodegeneration.

BRAP/Brap is a BRCA1 interacting protein that controls BRCA1's nuclear translocation (Li et al., 1998). We also identified BRAP as a key partner of NDE1 (nudE neurodevelopment protein 1), an essential molecule for human brain development and brain genome protection (Alkuraya et al., 2011; Bakircioglu et al., 2011; Houlihan and Feng, 2014; Lanctot et al., 2013). In addition, BRAP is a Ras-responsive ubiquitin E3 ligase that modulates the sensitivity of MAPK signaling (Matheny et al., 2004). Our previous studies showed that this role of Brap in neural progenitor cells (NPCs) was context-dependent and that Brap E3 ligase could act on both itself and other E3 ligases with wide nuclear substrates (Lanctot et al., 2013, 2017). These distinctive features allow Brap to serve as a liaison between the cell's microenvironment and cell nucleus to coordinate cell signaling, differentiation, and genome stability. Moreover, the essential role of Brap goes beyond brain development. In a recent genome-wide association study of 500,000 genotyped individuals along with information on their parents' age and cause of death, the *BRAP* gene locus was linked to the human lifespan (Timmers et al., 2019), suggesting an interplay between BRAP function and human aging.

By analyzing Brap null ($Brap^{-/-}$) and cerebral cortical NPC Brap conditional knockout ($Brap^{cKONPC}$) mice, we have shown that Brap loss of function (LOF) selectively affected the neuronal fate restrictive cell cycle of multipotent NPCs, exhibiting accelerated G1 phase, abrogated G1/S checkpoint, and prolonged S and G2 phases. The skewed cell cycle kinetics impeded the neurogenesis of NPCs and resulted in the reduced generation of cerebral cortical neurons (Lanctot et al., 2017). We now demonstrate that besides attenuating neurogenesis, Brap LOF also results in cellular senescence, affecting both NPCs and neocortical neurons. We show that senescence in $Brap^{-/-}$ and $Brap^{cKONPC}$ cells follows persistent DNA double-strand breaks (DSBs) and elevation of Brca1 as well as histone H2A mono- and poly-ubiquitination (H2Aub). Notably, the high H2Aub initiates proteasome-mediated H2A proteolysis, causing not only global epigenetic alteration but also increased proteasome burden. In the cortical tissue of $Brap^{cKONPC}$ mice, the backlog of polyubiquitinated proteins and SASP together results in neuroinflammation, neurodegeneration, and midlife mortality. We also demonstrate that H2Aub, the hallmark phenotype of Brap LOF, is elevated in cortical tissue of patients with AD. These results suggest that histone H2Aub is a key node connecting multiple aging hallmarks, highlighting an essential impact of chromatin aberrations on NDs.

RESULTS

Brap LOF results in accelerated cellular senescence with persistent DSBs

To understand the mechanism by which Brap LOF skews cell cycle kinetics and impedes the differentiation of NPCs, we isolated NPCs from $Brap^{-/-}$ embryos (before embryonic lethality by E13.5) and studied them in culture as neurospheres. Although $Brap^{-/-}$ NPCs grew at a rate comparable with their wild-type (WT) counterparts in the first 4–5 days *in vitro* (div), they abruptly ceased proliferation after 7–8 days (Figure 1A).

[13]Lead contact

*Correspondence:
yuanyi.feng@usuhs.edu

https://doi.org/10.1016/j.isci.2022.104519

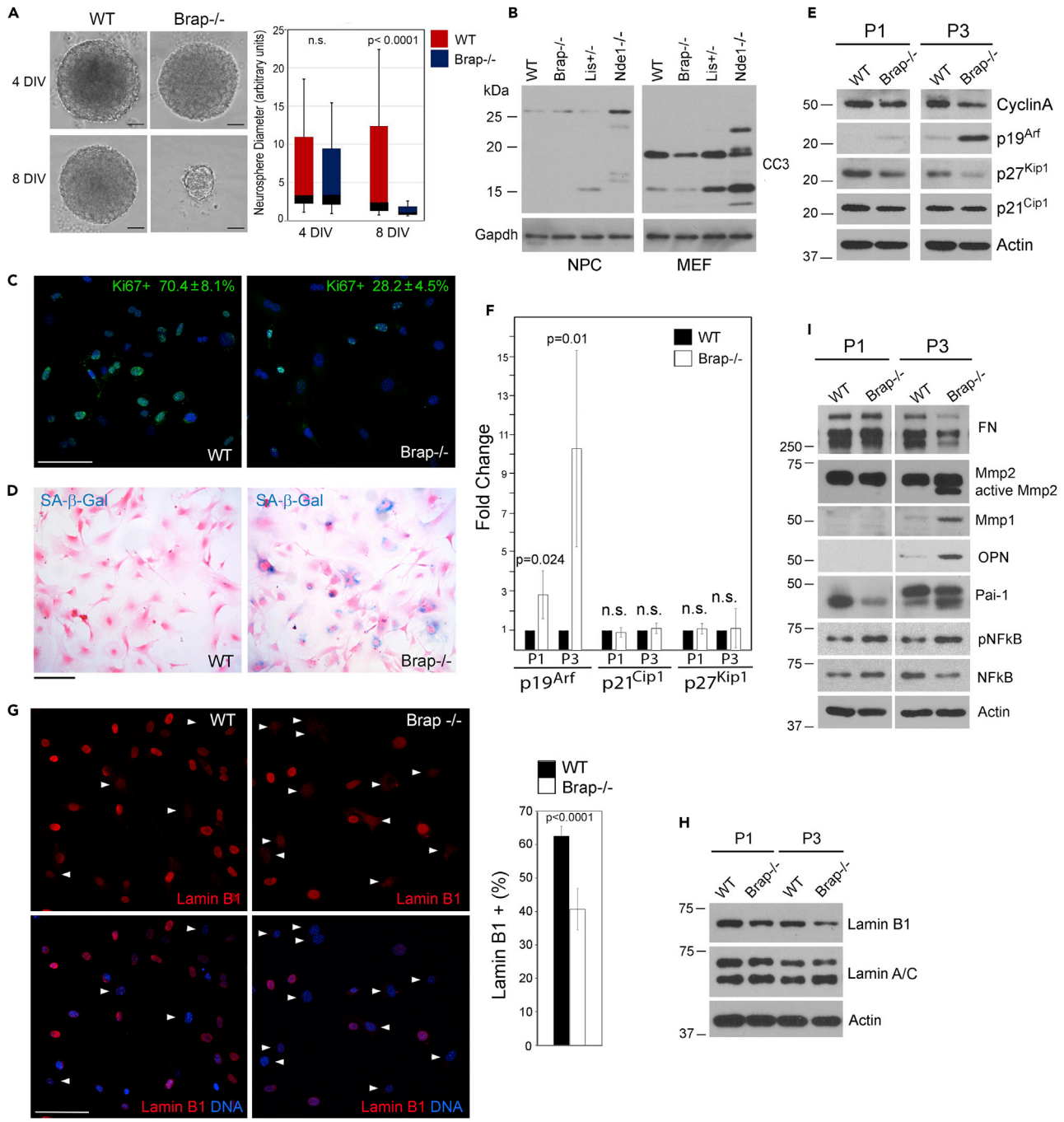

Figure 1. BRAP loss of function (LOF) results in accelerated cellular senescence

(A) Primary Brap$^{-/-}$ neural progenitor cells (NPC) cease growing in culture after 5–7 days *in vitro* (DIV). Shown are representative images of WT and Brap$^{-/-}$ neurospheres as well as box and whisker plots (Median ± Quartiles) of their diameter distribution at 4 and 8 DIV, respectively. p-values calculated by two-way ANOVA are indicated.

(B) Cleaved caspase 3 (CC3) immunoblotting of total protein extracts of primary NPCs and MEFs, respectively. Lis1$^{+/-}$ and Nde1$^{-/-}$ cells were used for CC3+ control as these cells were known to have high levels of apoptosis.

(C) Representative Ki67 immunofluorescence images of WT and Brap$^{-/-}$ MEFs at P2. The % of Ki67 + cells (Mean ± SD) is indicated.

(D) Senescence-associated β-gal assay of MEFs at P2, which indicates β-galactosidase activity (blue) in a higher fraction of Brap$^{-/-}$ cells. Cells were also counter-stained with eosin to view cell density and cell shape. Note the enlarged cell body of β-gal + cells.

(E and F) Immunoblotting and quantification (Mean ± SD) of G1/S CKIs in total protein extracts from MEFs at P1 (Passage 1) and P3, respectively. p-values calculated by Student's *t* test are indicated.

Figure 1. *Continued*

(G) Representative Lamin B1 immunofluorescence images and percentage (Mean ± SD) of Lamin B1+ MEFs at P2. p-values calculated by Student's *t* test are indicated. Cells showing a significant reduction of nuclear Lamin B1 are indicated by arrowheads.

(H) Immunoblotting of total protein extracts, showing reduced Lamin B1 in Brap$^{-/-}$ relative to WT MEFs at both P1 and P3.

(I) Immunoblotting of total protein extracts from MEFs at P1 and P3, showing increased SASP molecules in Brap$^{-/-}$ MEFs at P3. Note the increased Mmps and decreased Mmp substrate fibronectin (FN) in Brap$^{-/-}$ MEFs. Nuclear DNA was stained with Hoechst 33342. Bars: 100 um or as indicated.

This growth arrest was not accompanied by increased apoptosis (Figure 1B), which suggested that the mutant NPCs reached their replicative lifespan owing to cellular senescence.

To determine cellular senescence we turned to mouse embryonic fibroblast (MEFs) as they are better established for senescence analyses. We isolated MEFs from Brap$^{-/-}$ and WT embryos and cultured them following the 3T3 cell protocol (Todaro and Green, 1963). As expected, a greater fraction of Brap$^{-/-}$ MEFs showed multiple essential characteristics of cellular senescence as early as passage 2 (P2). These include an enlarged cell body, high senescence-associated beta-galactosidase (SA-β-gal) activity, loss of the Ki67 proliferation marker, and upregulation of p19^{Arf}, a CKI encoded by the p16^{Ink4a} locus that is alternatively transcribed and can act together with p16^{Ink4a} to induce cellular senescence (Capparelli et al., 2012; Haber, 1997; Quelle et al., 1995) (Figures 1C–1F). We further validated the senescence phenotype of Brap LOF by examining the loss of Lamin B1, another characteristic of cellular senescence (Freund et al., 2010). Both immunofluorescence (IF) and immunoblotting (IB) analyses demonstrated that Lamin B1 was downregulated much more rapidly in Brap$^{-/-}$ than WT MEFs from P1 to P3 (Figures 1G and 1H). To acquire the ultimate proof of cellular senescence, we assessed several known SASP molecules, including Mmp1, Mmp2, Serpin1 (Pai1), and Osteopontin/Spp1 (OPN) (Aoshiba et al., 2013; Castello et al., 2017; Coppe et al., 2010; Flanagan et al., 2018; Ghosh and Capell, 2016; Pazolli et al., 2012; Rao and Jackson, 2016; Vaughan et al., 2017). We found that all of them were elevated in Brap$^{-/-}$ MEFs along with reduced Mmp substrate fibronectin and increased phosphorylation of NFkB p65^{S536}, a chief mediator for SASP (Salminen et al., 2012) (Figure 1I). The multiple essential features of cellular senescence shown by Brap$^{-/-}$ cells demonstrate unambiguously that accelerated cellular senescence is a consequence of Brap LOF. These data also suggest that a pro-senescence fate change is at least partially responsible for impairing neuronal differentiation of Brap$^{-/-}$ NPCs in cortical development.

Whereas senescence is essentially a stress response to a variety of insults, we found that cellular senescence caused by Brap LOF follows persistent DNA damage responses (DDRs). First, we detected significant elevation of phospho-p53, -Atm, -Atr, and 53BP1 in Brap$^{-/-}$ MEFs before senescence was evident at P1 (Figures 2A–2C). In addition, a large fraction of Brap$^{-/-}$ MEFs showed persistent DNA damage foci with high levels of γH2A.X, the hallmark of DNA DSBs, and 53BP1, a marker for DSB repair (Panier and Boulton, 2014; Thiriet and Hayes, 2005) (Figures 2D–2F). Notably, the large γH2A.X and 53BP1 foci were in both proliferating (Ki67+) cells and cells that had ceased dividing (Ki67-) (Figures 2D and 2E, high magnification panels), indicating that DSBs occurred in Brap$^{-/-}$ cells both before they entered the senescent state and after they underwent replication arrest. Furthermore, we found that the persistent DSBs and rapid progression to senescence of Brap$^{-/-}$ MEFs coincided with increased levels of γH2A.X ubiquitination (Figure 2F). Whereas mono-ubiquitination of histone H2A is a DNA damage response, the ubiquitinated moiety of γH2A.X has been shown to mark non-apoptotic DSBs induced by oxidative DNA damage (Luczak and Zhitkovich, 2018). Consistent with this, we found that ubiquitin-modified γH2A.X (γH2A.Xub) in Brap$^{-/-}$ cells was further enhanced by H_2O_2 (Figure 2F), suggesting that γH2A.Xub is an apoptosis-evading and senescence-prone DNA damage response of Brap LOF.

Cellular senescence resulting from DSBs in cerebral cortical tissue underlie shortened lifespan of Brap^{cKONPC} mice

We subsequently found accelerated cellular senescence resulting from DSBs can also occur in the brain, causing shortened lifespan of mice in which Brap was conditionally ablated in NPCs of the dorsal telencephalon by the Emx1-Cre. In these Brap conditional knockout (cKO) mice (Brap$^{flox\ Emx1Cre+}$, referred to as Brap^{cKONPC} hereafter), Cre-mediated deletion results in Brap LOF in glutamatergic neurons, astroglia, and oligodendrocytes of the cerebral cortex (Gorski et al., 2002). We followed a cohort of adult Brap^{cKONPC} mice (n = 46) and their Brap$^{flox/WT}$ or Brap$^{flox/flox}$ Cre-control littermates (n = 29) over 12 months. We found that most Brap^{cKONPC} mice die between four and eight months with a median lifespan of six months (Figure 2G), whereas the average lifespan of mice is 2 years. The mutant mice lost weight, became lethargic,

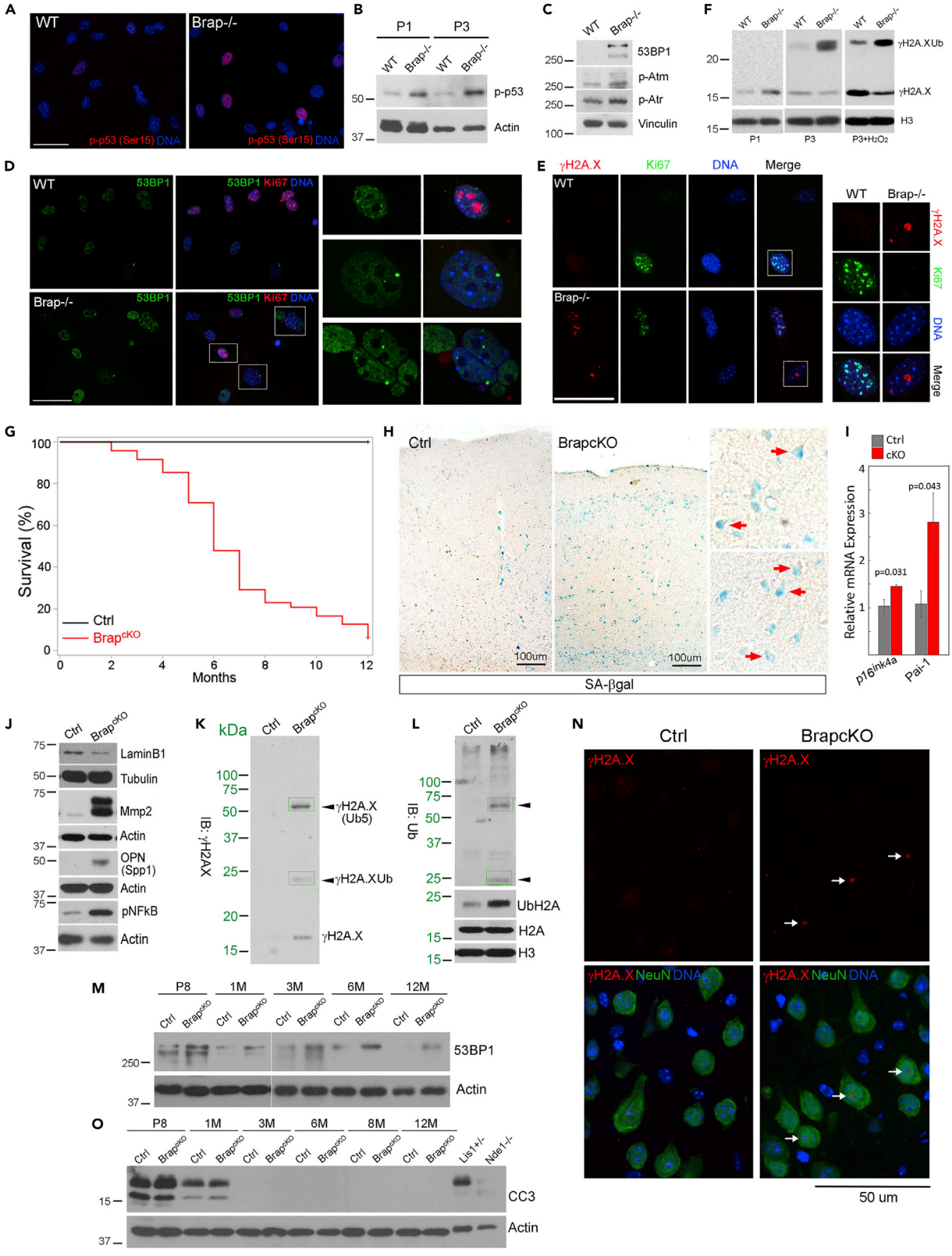
A
WT
Brap-/-
p-p53 (Ser15) DNA
B
P1
P3
WT
Brap-/-
p-p53
Actin
C
53BP1
p-Atm
p-Atr
Vinculin
F
γH2A.XUb
γH2A.X
H3
P1
P3
P3+H2O2
D
53BP1
53BP1 Ki67 DNA
E
γH2A.X
Ki67
DNA
Merge
G
Survival (%)
Months
Ctrl
BrapcKO
H
Ctrl
BrapcKO
100um
SA-βgal
I
Ctrl
cKO
Relative mRNA Expression
p=0.043
p=0.031
p16Ink4a
Pai-1
J
LaminB1
Tubulin
Mmp2
Actin
OPN (Spp1)
pNFkB
K
kDa
IB: γH2AX
γH2A.X (Ub5)
γH2A.XUb
γH2A.X
L
IB: Ub
UbH2A
H2A
H3
M
P8
1M
3M
6M
12M
53BP1
Actin
N
Ctrl
BrapcKO
γH2A.X
γH2A.X NeuN DNA
50 um
O
8M
Lis1+/-
Nde1-/-
CC3
Actin

Figure 2. Increased DSB and DDR are associated with cellular senescence in BRAP-deficient cells and cerebral cortices

(A) Representative images of phospho-p53 immunofluorescence staining of WT and Brap$^{-/-}$ MEFs at P2.

(B) Immunoblotting of total protein extracts from WT and Brap$^{-/-}$ MEFs at P1 and P3, respectively.

(C) Immunoblotting of DNA damage response (DDR) proteins in WT and Brap$^{-/-}$ MEFs at P1.

(D) Representative images of double immunofluorescence staining of WT and Brap$^{-/-}$ MEFs at P3 with antibodies against Ki67 (red) and 53BP1 (green).

(E) Representative images of double immunofluorescence staining of WT and Brap$^{-/-}$ MEFs at P3 with antibodies against Ki67 (green) and γH2A.X (red).

(F) Immunoblotting analyses of histone extracts of MEFs at P1 or P3, showing increased γH2A.X and γH2A.X mono-ubiquitination in Brap$^{-/-}$ MEFs.

(G) Kaplan–Meier curve shows significantly shortened lifespan ($p < 0.0001$ by log rank test) of Brap^{cKONPC} mice ($n = 46$) relative to their littermate control mice ($n = 29$).

(H) Representative images of senescence-associated β-gal analysis of cerebral cortical sections from Brap^{cKONPC} and control mice at three months of age. Note the pyramidal neuronal morphology of some SA-β-gal + cells (red arrows) in high magnification views.

(I) RT-qPCR shows an increased expression of p16^{Ink4a} and Pai-1 (plasminogen activator inhibitor-1/Serpine1) in three-month-old Brap^{cKONPC} cortices (Mean ± SD; $n = 4$ biological replicates). p-values calculated by Student's t test are indicated.

(J) Immunoblotting of cerebral cortical total protein extracts, demonstrating higher levels of senescence and SASP-like changes in the cortical tissue of Brap^{cKONPC} relative to littermate control mice.

(K and L) Immunoblotting of histone extracts from cortical tissue of three-month-old Brap^{cKONPC} and control mice, showing elevated γH2A.X as well as the presence of mono- and poly-γH2A.X ubiquitination in Brap^{cKONPC} mice (boxed bands). K and L are the same immunoblot that was first probed by anti-γH2A.X, stripped, and re-probed by anti-ubiquitin.

(M) Immunoblotting of total protein extracts from cortical tissue of Brap^{cKONPC} and control mice, showing persistent elevation of 53BP1 in Brap^{cKONPC} cortices from P8 (postnatal day 8) to 12M (12 months).

(N) Representative images of γH2A.X-NeuN double immunohistological staining of cerebral cortical sections from 4-month old WT or Brap^{cKONPC} mice. The presence of γH2A.X immunoreactivity in Brap^{cKONPC} neurons is indicated by arrows.

(O) Immunoblotting of total protein extracts from cortical tissue of Brap^{cKONPC} or control mice at various ages, showing that Brap LOF does not increase cleaved caspase 3, an apoptosis marker. Embryonic Lis1$^{+/-}$ and Nde1$^{-/-}$ cortical tissues were used as positive controls for the presence of apoptosis. Nuclear DNA was stained with Hoechst 33,342. Bars: 50 um or as indicated.

and showed slow or labored breathing when death became imminent. Therefore, Brap LOF in the cerebral cortex can accelerate aging and shorten the lifespan.

With midlife mortality, Brap^{cKONPC} mice showed high levels of cellular senescence in the cerebral cortical tissue. We first examined SA-β-gal activity in cortical sections. We found it was not only higher in Brap^{cKONPC} than in control mice but also shown by many mutant cells with pyramidal neuron morphology (Figure 2H, arrows). This suggested that, despite being replication-incompetent, neurons can undergo additional senescence-associated changes owing to Brap LOF. Further corroborating the increased cellular senescence, the cortical tissue of Brap^{cKONPC} mice showed upregulated p16^{Ink4}, decreased Lamin B1, and elevation of SASP factors including Serpin1 (Pai-1), Mmp2, Ssp1 (OPN), and phospho-NFkB (Figures 2I and 2J).

Similar to the observations in Brap$^{-/-}$ MEFs, increased cell senescence in Brap^{cKONPC} cortical tissue was associated with DSBs. We found that γH2A.X was not only elevated in the cortical tissue of Brap^{cKONPC} compared with control mice but also mono- and poly-ubiquitinated, showing a dominant pool of approximately 60 kDa that is equivalent to the molecular weight of γH2A.X with Penta-ubiquitin conjugations (Figures 2K and 2L). Such histone posttranslational modifications (PTM) with dual phosphorylation and poly-ubiquitination of H2A.X has not been reported before but appears to be characteristic of Brap^{cKONPC} cortical tissue in response to DSBs. Coinciding with increased γH2A.X, Brap^{cKONPC} cortical tissues also showed higher levels of 53BP1 (Figure 2M). Our immunohistological (IH) analysis further demonstrated that γH2A.X immunoreactivities were restricted to the nucleus of cortical neurons (NeuN+) but absent in glia (NeuN-) of Brap^{cKONPC} brains (Figure 2N). Given that we did not observe tumors or elevated apoptosis in the brain Brap^{cKONPC} mice (Figure 2O), cellular senescence is likely the main consequence of persistent DSBs and accounts for the premature mortality of Brap^{cKONPC} mice.

Transcriptomic profiles of Brap^{cKONPC} cortices reveal SASP candidates, immune activation, and impaired synaptic signaling

Compared with apoptosis, senescence following unsuccessful DSB repair is more deleterious *in vivo*, as senescent cells are stably viable and can chronically influence neighboring cells by secreting soluble molecules or by altering cell surface and extracellular matrix (ECM) proteins. The senescence-associated secretome varies with tissue and pathophysiological context but has not been investigated in the brain. We thus assessed the cerebral cortical SASP profile by identifying genes upregulated by Brap LOF. RNA sequencing (RNA-seq) was carried out with cerebral cortical total transcripts of Brap^{cKONPC} and littermate

control mice three months old. We identified 811 differentially expressed genes (DE-Gs) between the Brap^{cKONPC} and the control group, and of these, 373 genes were significantly upregulated by Brap LOF (Figure 3A and Table S1: RNA-seq Data Table). Consistent with the pro-inflammatory feature of cellular senescence, we found that 67 of the upregulated genes encode molecules associated with cells of the immune system and/or regulators of the innate immunity (Figure 3B). The upregulation of these genes indicates inflammatory responses in the mutant brain tissue. Moreover, 80 upregulated genes encode secreted molecules, which represent the cerebral cortical secretome of Brap^{cKONPC} mice. Increased expression of these molecules can pose non-cell autonomous tissue-wide effects. These SASP candidate genes include not only immune active molecules and proteases but also diverse neuropeptide neurotransmitters and peptide hormones with potent activities in neural networking and cerebrovascular regulation (Figure 3C). An additional 83 upregulated genes encode plasma membrane and ECM proteins that interface cells with their environment (Figure 3D). Increased expression of these genes can alter intercellular communication and tissue homeostasis. The most significantly upregulated genes in Brapc^{KONPC} cortices also include regulators for neurotransmitter metabolism, fatty acid and cholesterol metabolism, protein synthesis and sorting, as well as calcium homeostasis (Figure 3A and Table S1: RNA-seq Data Table). These molecular activities can have large effects, resulting in a global alteration in brain immunity and neural function.

Brap LOF also resulted in decreased expression of 438 genes in the cortical tissue (Table S1: RNA-seq Data Table). Notably, the most significant downregulation occurred in genes that play key roles in regulating energy homeostasis, neuronal activity, synaptic plasticity, neuronal excitatory-inhibitory balance, Wnt signaling, retinoid metabolism, as well as the production, secretion, and activity control of neuropeptides or neurotransmitters (Figure 3A). We performed Gene Ontology (GO) enrichment analysis of the 50 most significantly downregulated genes in Brap^{cKONPC} cortices. The GO terms identified in the BP category include impaired biological functions mainly in synaptic transmission as well as in cellular responses to stimuli and neuronal morphogenesis (Figure 3E), suggesting declining neuronal activity and plasticity. Overall, our transcriptomic data provide additional support for the impact of neuronal DSBs and cellular senescence on neuroinflammation and neural dysfunction of Brap^{cKONPC} mice.

Neuroinflammation and neurodegeneration in Brap^{cKO} brains

Inflammatory reactions in the cortical tissue are not only characteristics of cellular senescence but also contributors to neurodegeneration. We thus asked whether neurodegeneration is an outcome of DSBs and cellular senescence in Brap^{cKONPC} mice. As expected, neuroinflammatory and neurodegenerative phenotypes were readily detectable in Brap^{cKONPC} cortices starting at three months and progressing rapidly with age. First, hyperphosphorylation of the microtubule-associated protein tau became significantly increased in the cortical tissue of Brap^{cKONPC} mice at three months and was further elevated as the mutant mice grew older (Figures 4A and 4B). Increased tau phosphorylation in Brap^{cKONPC} cortices was found on multiple residues including T181, S202/T205, T217, T231, S396, and S416 (Figure 4A). The hyperphosphorylation of these residues is known to be associated with insoluble tau aggregates and neurodegenerative diseases (Augustinack et al., 2002). At the ages of six months or older, IH analysis with a phospho-tau T231 antibody revealed intense phospho-tau aggregates in the soma of some cortical neurons of Brap^{cKONPC} mice, and mutant neurons with this high soma phospho-tau T231 accumulation also frequently displayed deformed and/or eccentric nuclei (Figures 4C and S1A). As both T217 and T231 are considered early biomarkers for human AD and the phospho-tau T231 antibody labels all stages of neurofibrillary tangles (NFT) in human AD (Augustinack et al., 2002; Jicha et al., 1997; Suarez-Calvet et al., 2020), the presence of these human tauopathy-like changes in Brap^{cKONPC} mice suggested neurodegenerative brain dysfunction.

We further found astrogliosis and microgliosis were markedly elevated in Brap^{cKONPC} cortical tissue in an age-dependent fashion. Increased expression of glial fibrillary acidic protein (Gfap), which represents astrocyte activation, was undetectable in the cerebral cortex of Brap^{cKONPC} mice until about three months of age, and it then further progressed and became remarkably high as the mutant mice aged rapidly (Figures 4D, 4E and S1B). Parallel to astrogliosis was the strong increase in microgliosis in Brap^{cKONPC} cortices. As the brain's resident innate immune cells, microglia remain in a ramified resting state in healthy brains and are activated by injury or pathological processes. Analyses with pan-microglia marker Iba and activated phagocytic microglia marker CD68 both showed that microglia in Brap^{cKONPC} cortices were de-ramified, amoeboid-like, and activated (Figure 4F). To confirm neuroinflammation, we examined the expression of several key inflammatory molecules implicated in human NDs and our RNA-seq data (Dewachter et al., 2002; Frost et al., 2019; Newcombe et al., 2018; Sarlus and Heneka, 2017), including

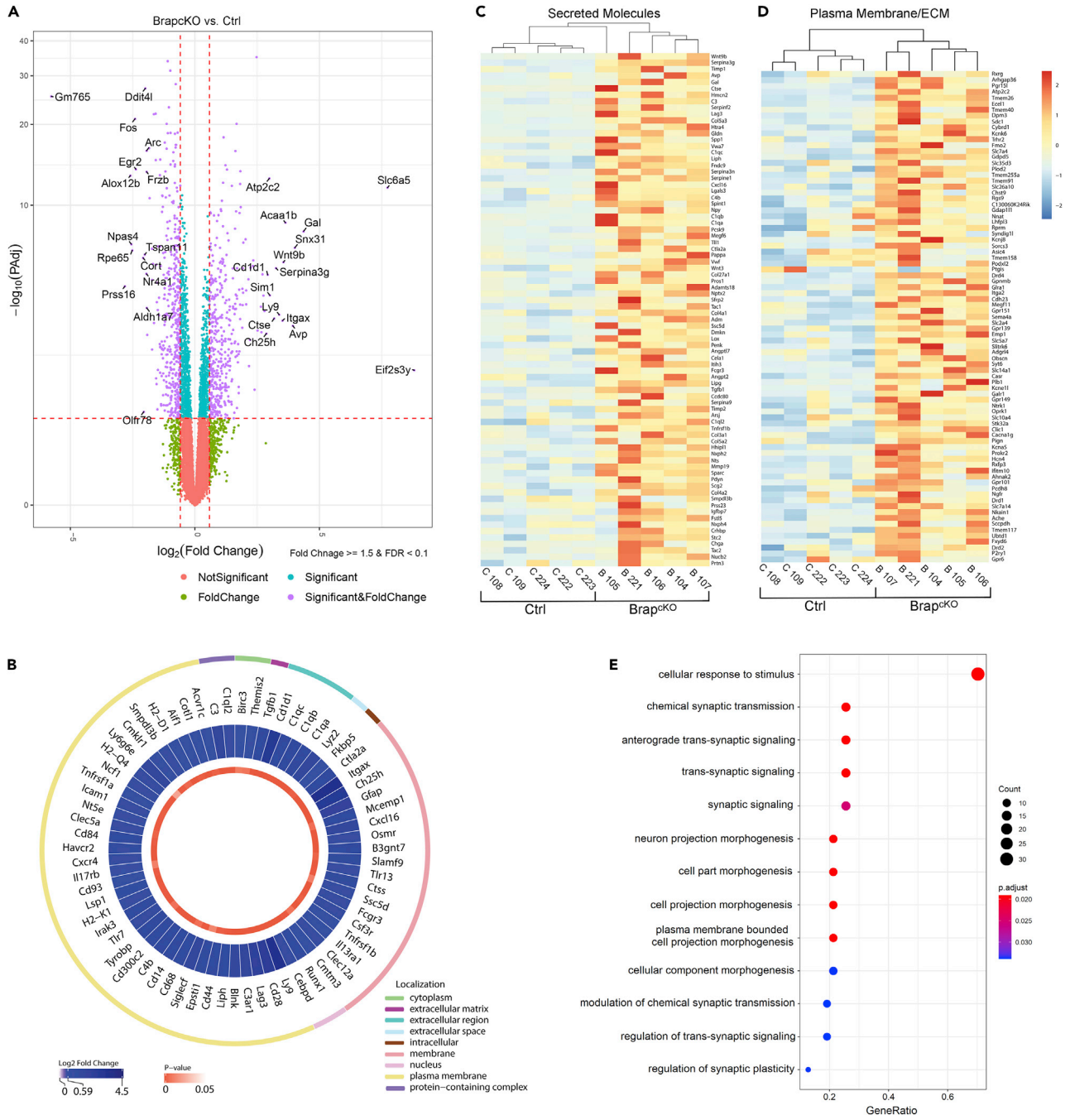

Figure 3. Differential gene expression caused by BRAP LOF reveals increased immune activities, SASP profiles, and compromised synaptic function in the cerebral cortical tissue

(A) Volcano plot shows differentially expressed genes (DE-Gs) between Brap^{cKONPC} and control cortical tissues.

(B) Circos plot presentation of upregulated genes associated with immune cells and innate immunity regulations in Brap^{cKONPC} relative to control cerebral cortices.

(C) Heatmap shows increased expression of genes encoding secreted molecules in Brap^{cKONPC} relative to control cerebral cortices.

(D) Heatmap shows increased expression of genes encoding plasma membrane and extracellular matrix molecules in Brap^{cKONPC} relative to control cerebral cortices.

(E) Gene ontology (GO) enrichment analysis of the top 50 down-regulated genes (by the adjusted p-value) in Brap^{cKONPC} relative to control cortical tissues. Shown are dot plots of biological processes affected by Brap LOF. Note that synaptic signaling, transmission, and cellular response are significantly compromised in Brap^{cKONPC} cortices.

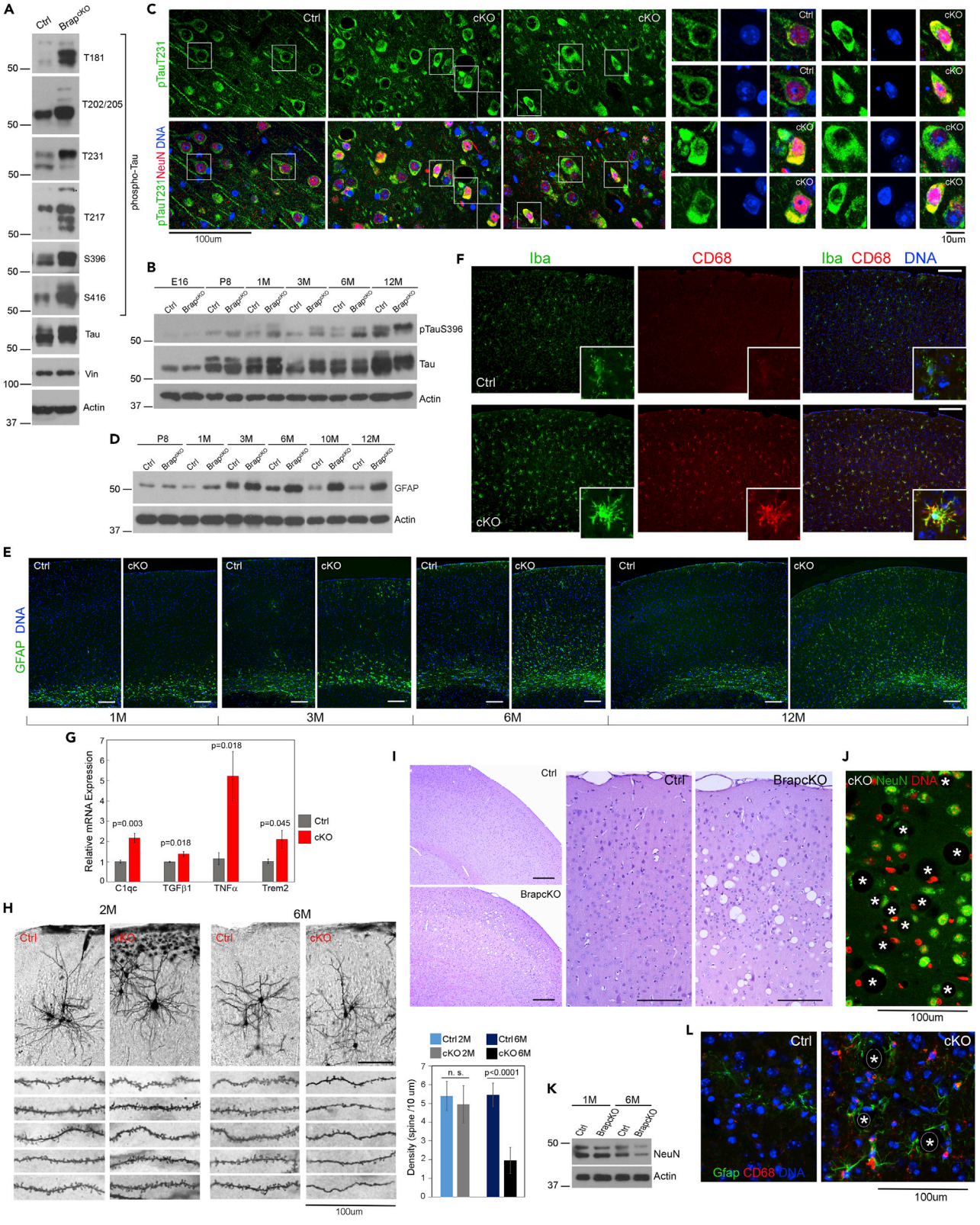
A
Ctrl
BrapcKO
T181
T202/205
T231
T217
S396
S416
phospho-Tau
Tau
Vin
Actin
50
100
37
B
E16
P8
1M
3M
6M
12M
pTauS396
Tau
Actin
C
pTauT231
pTauT231 NeuN DNA
Ctrl
cKO
100um
10um
D
GFAP
Actin
E
GFAP DNA
1M
3M
6M
12M
F
Iba
CD68
Iba CD68 DNA
G
Relative mRNA Expression
p=0.003
p=0.018
p=0.018
p=0.045
C1qc
TGFβ1
TNFα
Trem2
H
2M
6M
100um
I
BrapcKO
J
cKO NeuN DNA
100um
K
Ctrl 2M
cKO 2M
Ctrl 6M
cKO 6M
n. s.
p<0.0001
Density (spine /10 um)
NeuN
Actin
L
Gfap CD68 DNA
100um

Figure 4. BRAP LOF in cerebral cortical NPCs results in neuroinflammation and accelerated neurodegeneration

(A) Immunoblotting of cerebral cortical total protein extracts from three-month-old Brap^{cKONPC} and control mice with various anti-phospho-tau antibodies.

(B) Immunoblotting of cortical total protein extracts shows age-dependent progression of tau hyperphosphorylation (on S396) in Brap^{cKONPC} cortices.

(C) Double immunohistological staining with anti-phospho-tau T231 (green) and anti-NeuN (red) antibodies shows marked increase in phospho-tau in the cerebral cortex of Brap^{cKONPC} mice at 11 months. Shown are representative images. Note the co-occurrence of intense phospho-tau aggregates in the soma and the deformed nuclei of mutant cortical neurons at higher magnifications.

(D and E) Gfap immunoblotting and immunohistological analyses show the age-dependent progression of astrogliosis in Brap^{cKONPC} cortices.

(F) Double immunohistological staining with anti-Iba (green) and anti-CD68 (red) antibodies shows marked increase in microglia activation in Brap^{cKONPC} cortices at three months. Representative images are shown.

(G) RT-qPCR analyses of selected neuroinflammatory genes in three-month cortical tissues (Mean ± SE; *n* = four to eight biological replicates). p-values calculated by Student's *t* test are indicated.

(H) Representative images and quantification (Mean ± SD) of Golgi-cox analyses, showing significantly reduced density of dendritic spines in cortical layer 2/3 pyramidal neurons of Brap^{cKONPC} mice at six months. p-values calculated by Student's *t* test are indicated.

(I) H&E stained brain sections of 10-months-old Brap^{cKONPC} and control mice, showing spongiform encephalopathy in Brap^{cKONPC} cortical gray matter.

(J) A representative NeuN immunohistological image shows a reduced neuronal density and dystrophic or distorted neurons adjacent to spongiosis (positions of vacuoles are marked by asterisks).

(K) Immunoblotting of cortical total protein extracts, demonstrating decreased NeuN in Brap^{cKONPC} cortices at six months.

(L) Representative Gfap (green) and CD68 (red) double immunohistological images, showing increased astrogliosis and microgliosis surrounding the spongiform vacuoles (positions of vacuoles are marked by asterisks). Nuclear DNA was stained with Hoechst 33342. Bars: 100 um or as indicated. See also Figure S1.

C1q, TNFα, TGFβ1, and Trem2. All of them were upregulated significantly in the cortical tissue of three-month-old Brap^{cKONPC} mice relative to that of control mice (Figure 4G). The strong astrocyte and microglial activation along with increased inflammatory cytokines in Brap^{cKONPC} cortical tissue were in line with RNA-seq data, and they together demonstrate the neuroinflammatory and neurodegenerative brain dysfunction of Brap^{cKONPC} mice.

To ascertain Brap LOF leads to neurodegeneration, we examined the brain structure of Brap^{cKONPC} mice that survived to six months or older. We first performed a Golgi-Cox stain to reveal the morphology of cortical neurons. Whereas neurons in Brap^{cKONPC} brains were grossly normal in dendritic and axonal morphology, the density of their apical dendritic spines was significantly decreased in cortical layer II/III pyramidal neurons compared with those in wild type or control mice, whereas changes in dendritic spine density were insignificant in mutant mice of younger ages (Figure 4H). These results fully agreed with the impaired synaptic transmission and neuronetwork activities in Brap^{cKONPC} mice revealed by RNA-seq, further supporting an age-dependent decline in cortical neuronal functions.

To assess whether there is an age-dependent neuronal loss in Brap^{cKONPC} mice, we examined H&E-stained brain sections of a set of Brap^{cKONPC} mice (*n* = 12) that survived to six months or older. We found all mutant brains showed spongiform encephalopathy in the cortical gray matter (Figure 4I). The spongiform changes were widespread, resulting in striking neuronal soma deformation and vacuolization (Figures 4J and S1C). Whereas spongiform encephalopathy is characteristic of prion diseases, it was absent in younger Brap^{cKONPC} mice or control littermates, not accompanied by the accumulation of the prion protein Prp (Figure S1D), but was associated with a loss of cortical neurons (Figure 4K). These indicated that it was a non-infectious neurodegenerative lesion. Many spongiform vacuoles in Brap^{cKONPC} cortices were surrounded by reactive astrocytes and microglia (Figure 4L), suggesting their association with chronic neuroinflammation in promoting neurodegenerative pathology.

As DSBs in Brap^{cKONPC} mice are neuronal-specific, we tested whether this neuronal defect accounts for the multitude of phenotypes involving both neurons and glia in Brap^{cKONPC} mice. We generated a Brap neuronal conditional knockout line by abrogating Brap in neurons of the postnatal cortex and hippocampus with a Thy1-Cre driver (Dewachter et al., 2002) (Brap$^{flox\ Thy1Cre+;}$ referred to as Brap^{cKONeuron}), and asked whether Brap LOF in neurons could recapitulate the phenotype of Brap LOF in NPCs. About half of the Brap^{cKONeuron} mice (33 out of 63) were found dead by six months of age. Analyses of Brap^{cKONeuron} brains revealed phenotypes indistinguishable from those of the Brap^{cKONPC} mice with respect to increased DSBs, γH2A.Xub, cellular senescence, tau hyperphosphorylation, astrogliosis, and microgliosis (Figures S1E–S1J). This indicated that the astroglia and microglia activation in Brap^{cKONPC} mice were non-cell-autonomous responses to damaged neurons. The phenocopy of Brap^{cKONeuron} and Brap^{cKONPC} mice strongly supports the notion that sustained DSBs and senescence of cortical neurons can be a main source of neuroinflammation to induce neurodegeneration.

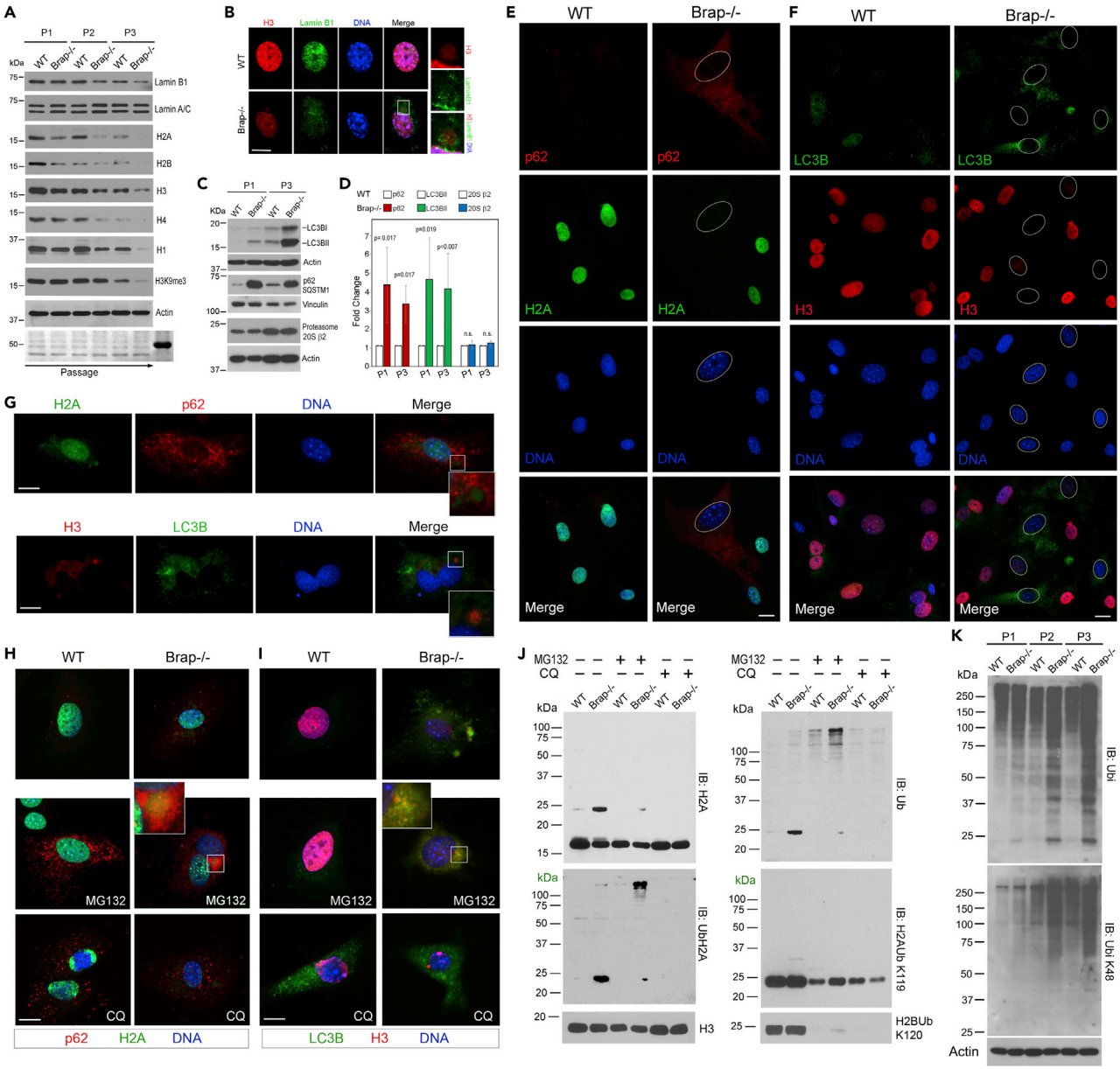

Figure 5. Cellular senescence in BRAP$^{-/-}$ MEFS was associated with histone H2A ubiquitination and UPS-mediated proteolysis

(A) Immunoblotting analyses of MEF total protein extracts, showing a progressive reduction of Lamin B1 and core histones with increased culture senescence.

(B) Representative immunofluorescence images of histone H3 (red) and Lamin B1 (green) double stained MEFs at P3, showing the presence of cytoplasmic Lamin B1 and histone in Brap$^{-/-}$ MEFs (boxed area at higher magnification).

(C) Immunoblotting analyses of autophagy markers LC3B and p62, as well as 20S proteasome catalytic β2 subunit, showing increased autophagy flux without alteration of proteasome abundance in Brap$^{-/-}$ relative to WT MEFs at both P1 and P3.

(D) Quantification (Mean ± SD) of p62, LC3BII, and 20Sβ2 levels in WT and Brap$^{-/-}$ MEFs at P1 and P3, respectively. n = 3–5 biological replicates. p-values calculated by Student's t test are indicated.

(E–G) Representative immunofluorescence images of WT and Brap$^{-/-}$ MEFs at P3. Antibodies against p62 (red) or LC3B (green) were used to identify autophagosome and co-stained with anti-histone H2A (green) or anti-histone H3 (red). Note that in Brap$^{-/-}$ MEFs, the reduction in nuclear histones coincides with the presence of cytoplasmic histone particles and increased p62 and LC3B but there is little cytoplasmic histone-autophagosome co-localization (boxed area at higher magnification of G).

(H and I) Representative immunofluorescence images of MEFs treated with UPS blocker MG132 or lysosome blocker chloroquine (CQ), showing that cytoplasmic H2A-p62 or H3-LC3B co-localization is enhanced by MG132 but not by CQ (boxed area at higher magnification).

Figure 5. *Continued*

(J) Immunoblotting analyses of histone extracts from MEFs at P2, showing Brap LOF caused elevated histone H2A mono- and poly-ubiquitination. The level of poly-H2Aub was further increased by MG132 but not by CQ, indicating UPS-mediated histone H2A proteolysis.

(K) Immunoblotting analyses of MEFs total protein extracts, demonstrating increased levels of polyubiquitinated proteins in senescent Brap$^{-/-}$ MEFs. Nuclear DNA was stained with Hoechst 33342. Bars: 10 um. See also Figure S2.

Cellular senescence is associated with histone H2A ubiquitination and histone proteolysis

DSBs, if unsuccessfully repaired, can lead to several alternative consequences including oncogenesis, apoptosis, and cellular senescence. To understand the mechanism by which DSBs selectively cause cellular senescence, we looked into γH2A.Xub, the unique DDR of Brap LOF (Figures 2F and 2K). γH2AX, formed by phosphorylation of the Ser-139 residue of the histone variant H2A.X, is an early response to DSBs, whereas mono-ubiquitination of histone H2A can also be a DDR that mediates DNA repair and transcriptional silencing (Uckelmann and Sixma, 2017; Wang et al., 2004). Thus, the co-occurrence of phosphorylation and ubiquitination of H2A.X, especially the poly-γH2A.Xub in Brap-deficient cells and tissues suggested a possibility of ubiquitin-mediated histone degradation, as global histone loss has been shown in aging and cellular senescence (Feser et al., 2010; Hu et al., 2014; Ivanov et al., 2013). In agreement with this possibility, we found all major histones were progressively depleted as MEFs underwent senescence, whereas Brap$^{-/-}$ MEFs lost histones more rapidly than the WT MEFs (Figure 5A). This rapid histone loss can decrease nucleosome occupancy and lead to global chromatin reconfiguration that may be necessary for Brap$^{-/-}$ cells to enter and persist in the state of senescence.

The loss of nuclear histones corresponded with the detection of cytoplasmic histone particles in Brap$^{-/-}$ MEFs. These cytoplasmic histone particles often did not contain DNA, but frequently co-occurred with the extrusion of Lamin B1 from the nucleus to the cytoplasm, whereas the nuclear envelope remained intact (Figures 5B and S2A–S2C). Lamin B1's cytoplasmic extrusion and clearance by the autophagy lysosome pathway (ALP) have been shown to mediate cellular senescence (Dou et al., 2015). Indeed, the autophagic flux was elevated in Brap$^{-/-}$ MEFs, as evidenced by the significantly higher level of autophagy markers LC3BII and p62/SQSTM1 in Brap$^{-/-}$ than in WT MEFs (Figures 5C and 5D). We also found that cells presenting stronger p62 and/or LC3B immunoreactivities were precisely those that showed reduced nuclear histones and cytoplasmic histone particles. However, immunoreactivities of cytoplasmic histone particles and p62 and/or LC3B showed little overlap (Figures 5E–5G), raising a possibility that histone clearance in Brap$^{-/-}$ MEFs was through the ubiquitin proteasome system (UPS) as suggested by the increased poly-γH2A.Xub.

To test UPS-dependent histone proteolysis, we blocked the proteasome activity with GM132 and re-examined the cytoplasmic histone particles. We found MG132 treatment enhanced the co-localization of cytoplasmic histone with p62 and LC3B in Brap$^{-/-}$ MEFs, whereas the lysosome inhibitor chloroquine (CQ) did not have this effect (Figures 5H and 5I). Therefore, the cytoplasmic histone particles in senescent Brap$^{-/-}$ MEFs were destined for UPS clearance. To verify the UPS-dependent histone proteolysis, we extracted histones from Brap$^{-/-}$ and WT MEFs and analyzed their UPS- or ALP-dependent ubiquitination state. We found that Brap LOF resulted in a specific increase in both mono- and poly-ubiquitinated histone H2A (mono- or poly-H2Aub). Inhibition of UPS, but not the lysosome, resulted in a simultaneous decrease in mono-H2Aub and an increase in poly-H2Aub (Figure 5J). This coupled reduction of mono-H2Aub with an elevation of poly-H2Aub suggested that mono-H2Aub in Brap$^{-/-}$ cells is destined for poly-H2Aub and proteasomal degradation. Therefore, UPS is primarily responsible for histone H2A proteolysis in Brap$^{-/-}$ cells, in which mono-H2Aub acts as a primer that may further progress to poly-H2Aub and histone degradation. Whereas H2Aub elevation was accompanied by the degradation of other histone molecules in Brap$^{-/-}$ MEFs, we did not detect ubiquitin-modifications histones H2B, H3, H4, and H1 (Figure S2D). Although it is possible that the levels of ubiquitin-modified H2B, H3, H4, and H1 were too low to be detected by antibodies against their native forms, these findings suggest other histones are degraded either alongside H2Aub without their own ubiquitin modifications or via UPS-independent mechanisms.

Histones are among the most abundant proteins in eukaryotic cells, and their increased proteolysis via UPS is likely to overwhelm the proteasome's capacity, decreasing the clearance of other UPS substrates while stimulating the autophagic flux. Supporting an increased UPS burden in Brap$^{-/-}$ MEFs, we found that the level and activity of proteasome 20S catalytic core complex were not significantly altered by Brap LOF (Figures 5C, 5D, and S2E), but there was a remarkable buildup of polyubiquitinated proteins as Brap$^{-/-}$ MEFs progressed to senescence (Figure 5K). Therefore, the depletion of histones and the accumulation

of polyubiquitinated cellular proteins in Brap$^{-/-}$ MEFs can together lead to the global epigenetic and metabolic alterations underlying the stable expression of a multitude of phenotypes that reinforce the senescence state.

H2A ubiquitination and BRCA1 activation are the hallmark phenotypes of Brap LOF

Because H2Aub is pivotal for initiating histone H2A proteolysis, we further evaluated whether it is a primary and early defect of Brap LOF by examining multiple tissues and ages of Brap mutant mice. We found H2Aub was significantly elevated in Brap$^{-/-}$ and Brap^{cKONPC} mice relative to their wild type and control counterparts regardless of cell types and ages (Figures 6A and S3A). Therefore, increasing the level of H2Aub is a hallmark phenotype of Brap LOF.

The ubiquitin modification of histone H2A is mediated by three major types of ubiquitin E3 ligases including the RNF168 and RNF8 RING-type E3 ligase, the Ring1A/B-Bmi1 polycomb repressive complex 1 (PRC1), and the BRCA1-BARD1 complex. These H2A E3 ligases modify H2A in a site-specific manner to facilitate DNA repair and promote chromatin compaction (Horn et al., 2019; Kalb et al., 2014; Mattiroli and Penengo, 2021; Tamburri et al., 2020; Uckelmann and Sixma, 2017). As BRAP interacts with BRCA1 directly and acts as a cytoplasmic docking protein to regulate BRCA1's nuclear-cytoplasmic balance (Li et al., 1998), we tested whether increased H2Aub in Brap-deficient cells and tissues was associated with altered Brca1. As expected, we found Brca1's abundance in Brap$^{-/-}$ MEFs, NPCs, embryos, and cortical tissues of Brap^{cKONPC} mice was consistently increased in comparison with WT and control cells or tissues (Figure 6B). In addition, we found the nuclear pool of Brca1 was much higher in Brap$^{-/-}$ than in WT cells (Figure 6C). The high level of nuclear Brca1 was also shown by cortical neurons of the Brap^{cKONPC} mice (Figures 6D and S3B). These data not only indicated that increasing Brca1's nuclear abundance is another hallmark phenotype of Brap LOF but also suggested that the Brca1 ubiquitin E3 ligase activity is at least partially responsible for the increased H2Aub resulting from Brap LOF.

The BRCA1 E3 ligase activity, though it may act independently of DSB repair, is integral to BRCA1's role in tumor suppression (Wu et al., 2009). The substrate of BRCA1 E3 ligase includes both canonical H2A and H2A variants (Kim et al., 2017). In the cortical tissue of Brap^{cKONPC} mice, we found H2A.X and H2A.Y were also ubiquitinated at higher levels relative to that of the control mice (Figures 6E and S3C). This provided additional support for Brca1 as a key player in increasing H2Aub in Brap-deficient cells and tissues.

The ubiquitination of H2A by BRCA1 is thought to be at the C-terminal tail on K125/127/129 (Uckelmann and Sixma, 2017). As antibodies for these site-specific modifications are lacking, we performed IBs with an available ubiqutyl-H2A monoclonal antibody, which reportedly recognizes H2Aub at K119 (Jullien et al., 2017; Taherbhoy et al., 2015). H2Aub on K119 is the most prevalent form of H2Aub. This is predominantly catalyzed by PRC1 that mediates chromatin compaction, polycomb gene repression, and plays a role in neurodegeneration (Abdouh et al., 2012; El Hajjar et al., 2019; Liu et al., 2014; Srivastava et al., 2021; Wang et al., 2004). The H2AubK119 antibody showed significantly higher immunoreactivity to histones from cortical tissue of Brap^{cKONPC} mice than those from control mice after one month of age, yet the degree of upregulation in Brap^{cKONPC} cortical tissue revealed by pan-H2A antibodies was greater than was shown by the H2AubK119 antibody (Figures 5J, 6A, and S3A). This suggested that H2A in Brap-deficient cells and tissues is likely to be ubiquitinated at multiple sites. Although an altered level and nuclear localization of Ring1B, the catalytic component of the PRC1, were not detected in Brap$^{-/-}$ MEFs (Figure 6C), we observed a subtle-to-moderate elevation in the abundance of Ring1B and Bmi-1 of the PCR1 complex in older Brap^{cKONPC} than in control cortices (Figure S3D). As BRAP is a ubiquitin E3 ligase capable of modulating other E3 ligases with multiple downstream nuclear targets (Lanctot et al., 2017), it remains possible that Brap LOF affects H2Aub through both Brca1 and the PRC1 complex.

H2Aub is coupled with the loss of proteostasis in cerebral cortical tissue and is elevated in AD

To determine whether increased histone H2Aub can drive brain aging and promote neurodegeneration, we further examined the histone content, ubiquitinated protein levels, and protein homeostasis in cortical tissues of Brap^{cKONPC} mice. Reminiscent of senescent Brap$^{-/-}$ MEFs, increased mono-H2Aub in Brap^{cKONPC} cortices was accompanied by poly-H2Aub buildup and nuclear histone reductions in a subpopulation of cells (Figures 6F and 6G). We found cells showing weaker nuclear histone immuno-reactivity were surrounded by reactive astrocytes, supporting the notion that histone proteolysis stabilizes the senescent chromatin state and mediates the senescence-associated neuroinflammation. Also similar to what was

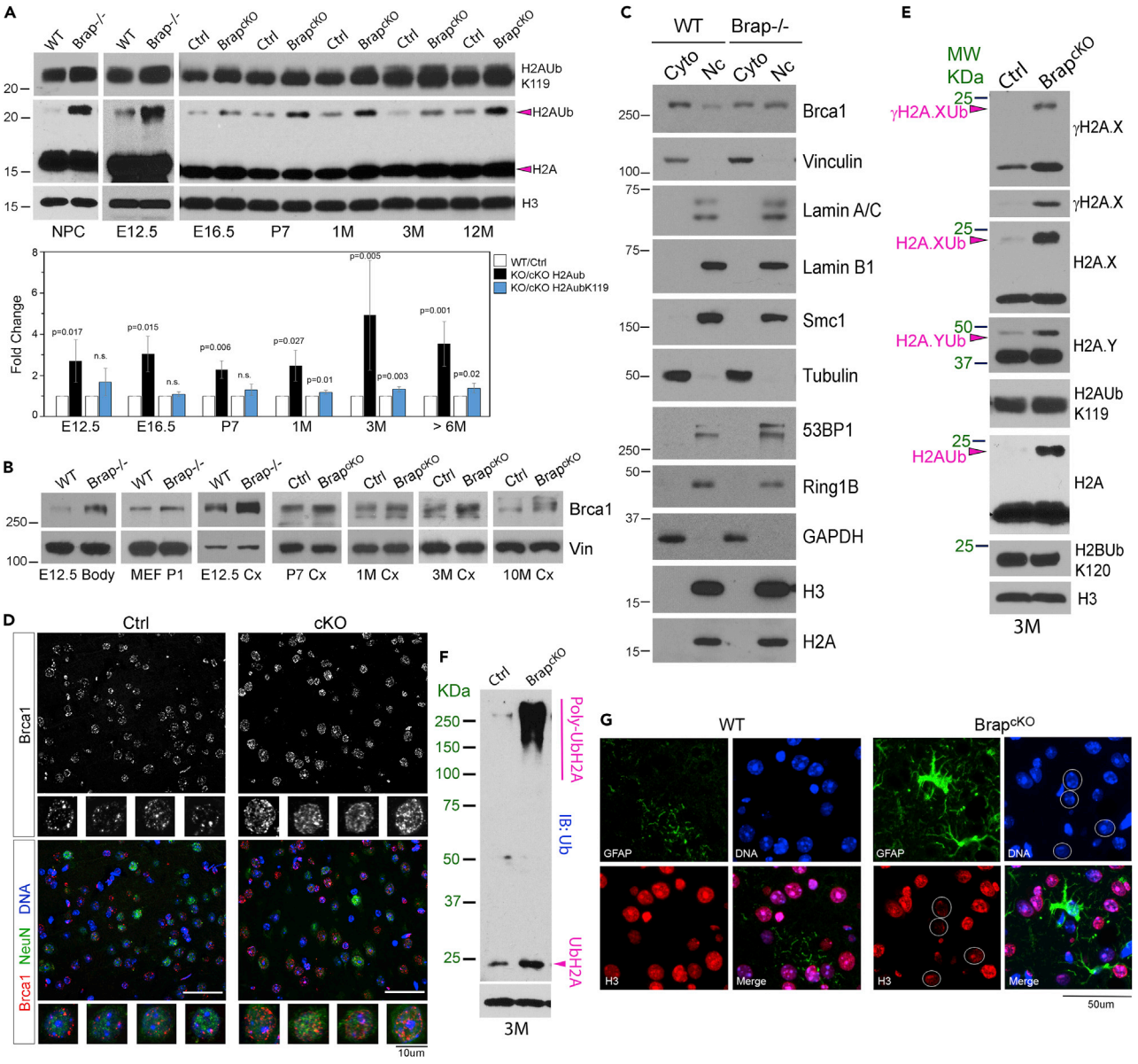

Figure 6. Histone H2A ubiquitination accompanied by BRCA1 activation is the hallmark phenotype of BRAP LOF

(A) Immunoblotting of histone extracts from NPCs as well as from embryonic, neonatal, adult cerebral cortical tissues, and quantification (Mean ± SD) of increases in histone H2Aub (total H2Aub and H2AubK119, respectively) resulted from Brap LOF. *n* = 3–6 biological replicates. p-values calculated by Student's *t* test are indicated.

(B) Immunoblotting of Brca1 in various cells and tissues, showing that Brap LOF results in increased Brca1 abundance.

(C) Immunoblotting of nuclear vs cytoplasmic fractions of MEFs at P1, showing increased nuclear localization of Brca1 in Brap$^{-/-}$ cells.

(D) Brca1 (red) and NeuN (green) double immunohistology images of cerebral cortical sections of Brap^{cKONPC} and control mice at four months of age. Representative images are shown. Note the increased intensity and density of Brca1 puncta in the nuclei of Brap^{cKONPC} cortical neurons (NeuN+).

(E and F) Immunoblotting analyses of histone extracts from cerebral cortical tissues of three-month-old mice, showing increased ubiquitination of H2A variants targeted by Brca1 (E) along with total histone H2A ubiquitination (F).

(G) Double immunohistology staining of cortical sections of 4-month old WT or Brap^{cKONPC} mice with antibodies against Gfap (green) and histone H3 (red), showing reduced nuclear histones in cells surrounded by reactive astrocytes (circles) in Brap^{cKONPC} cortical tissues. Representative images are shown. Nuclear DNA was stained with Hoechst 33342. Bars: 50 um or as indicated. See also Figure S3.

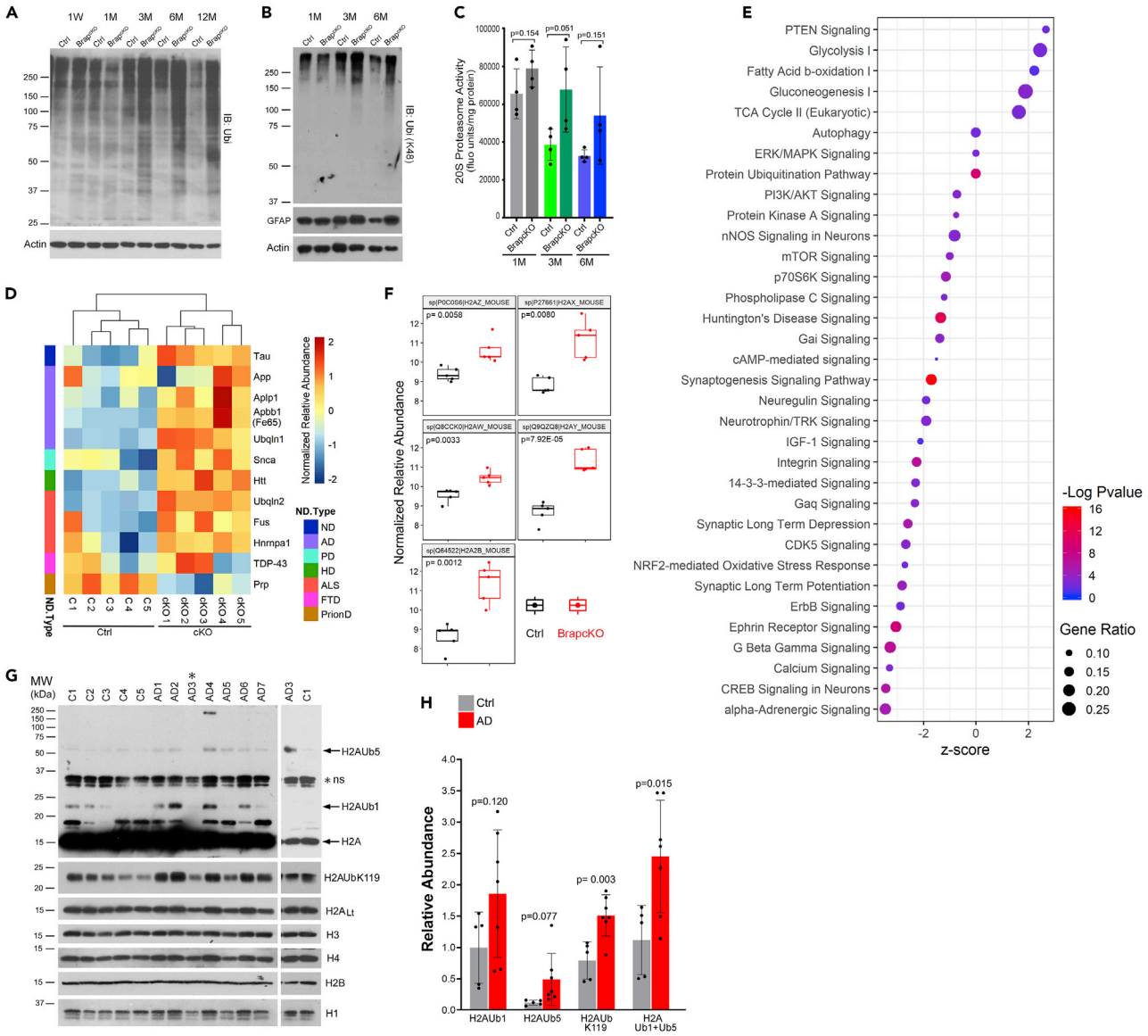

Figure 7. Impaired proteostasis resulting from BRAP LOF in cerebral cortical tissue overlaps with proteopathy of neurodegenerative disorders

(A and B) Ubiquitin immunoblots (total ubiquitination or K48-linked polyubiquitination) of cortical tissue total protein extracts from Brap^{cKONPC} and littermate control mice, demonstrating age-dependent accumulation of poly-ubiquitinated proteins in the mutant cortical tissues.

(C) 20S proteasome activities in the cortical tissue of Brap^{cKONPC} and control mice at one, three, and six months of age (Mean ± SD). p-values calculated by Student's *t* test are indicated.

(D) Heatmap of relative protein abundance shows selected proteins accumulated in aging Brap^{cKONPC} cortical tissue that are also implicated in proteopathy of human neurodegenerative disorders. ND, neurodegenerative disease; AD, Alzheimer's disease; PD, Parkinson's disease; HD, Huntington's disease; ALS, Amyotrophic lateral sclerosis; PD, Prion disease.

(E) Dot plot of signaling pathways altered by Brap LOF in aging cerebral cortical tissues. Shown were results of IPA of significantly altered proteins revealed by TMT analysis of Brap^{cKONPC} vs control cortical proteome.

(F) Box and whisker plots (Median ± Quartiles) of selected results of the TMT analysis, showing significant elevation of multiple histone H2A variants in Brap^{cKONPC} relative to control cortical tissues. p-values calculated by two-way ANOVA are indicated.

(G) Immunoblotting of histone extracts from postmortem cortical tissues of seven AD patients (AD1–AD7) and five age matched normal controls (C1–C5). Each blot was probed sequentially by various anti-histone antibodies including pan-H2A, H2AubK119, H3, H4, H2B, and H1. Shown were representative results of four technical replicates. AD3* denotes the AD3 isolate that was partially degraded. The frozen cortical tissue from this case was examined by multiple technical replicates and more representative results were shown by immunoblots on right panels and those on Figure S4 when degradation was minimized.

Figure 7. *Continued*

(H) Quantification (Mean ± SD) of the relative abundance of ubiquitinated histones H2A normalized to that of histone H3. p-values calculated by Student's *t* test are indicated. The demonstrates significant elevations in the level of histone H2A mono-ubiquitination detected by an antibody for H2AubK119 and the overall level of H2A ubiquitination (H2Aub1+ub5) detected by the pan-H2A antibodies in AD cortical tissues in comparison with the age-matched controls. See also Figure S4.

observed in Brap$^{-/-}$ MEFs, increased mono- and poly-H2Aub was accompanied by substantial elevation of the overall level of poly-ubiquitinated proteins in the Brap^{cKONPC} cortical tissue. Notably, in the cortex of Brap^{cKONPC} mice, the abundance of polyubiquitinated proteins was not obviously altered during embryonic and neonatal development, but started to elevate at young adult ages, then further built up progressively with age, and became remarkably high by six months of age (Figures 7A, 7B, S4A and S4B). Despite the substantial backlog of poly-ubiquitinated proteins, we did not detect decreased proteasomal activities in the mutant cortical tissues. Instead, aging Brap^{cKONPC} mice showed a tendency toward elevating the catalytic activity of 20S core proteasomal complex (Figure 7C). This demonstrates clearly that the age-dependent loss of proteostasis in Brap^{cKONPC} cortices was not owing to reduced UPS function but rather caused by the overproduction and backlog of polyubiquitinated proteins, among which H2Aub was the primary target resulting from Brca1-mediated DDR, whereas other polyubiquitinated proteins were owing to UPS overflow.

Because the progressive decline in proteostasis is a prominent hallmark of aging and a common pathological feature of neurodegeneration, we assessed the altered cortical proteome in aged Brap^{cKONPC} mice to evaluate whether it may resemble the proteopathy of NDs. We performed tandem mass tags (TMT) quantitative proteomics analysis of whole cortical proteins from six-month-old Brap^{cKONPC} and control mice. Out of the total 4,708 quantified proteins, the abundance of 903 proteins was significantly altered by Brap LOF (Table S2 TMT Proteomics Table). Notably, many toxic proteins associated with AD, Parkinson's disease (PD), Huntington's disease (HD), and Amyotrophic lateral sclerosis (ALS) were found to have accumulated in the Brap^{cKONPC} relative to the control cortical tissues (Figure 7D), which suggested overlapping pathogenesis between Brap LOF and human NDs. We further analyzed the alteration in proteomic profiles resulting from Brap LOF by testing their association with biological processes. In addition to aberrant protein ubiquitination and quality control, Ingenuity Pathway Analysis (IPA) showed that the cerebral cortex of Brap^{cKONPC} mice had altered glucose and fatty acid metabolism, deregulated nutrient sensing, as well as declines in numerous cell signaling pathways and neuronal network activities (Figure 7E). Notably, both long-term depression (LTD) and long-term potentiation (LTP) were significantly decreased in Brap^{cKONPC} cortices, indicating diminished synaptic plasticity and impaired cognition of the mutant brain (Figure 7E). These data demonstrated that the brain function of Brap^{cKONPC} mice was impaired at multiple levels before they die of premature brain aging and neurodegeneration.

With the remarkable proteomic alteration, multiple components of the 19S proteasome regulatory particles were significantly upregulated in Brap^{cKONPC} relative to control cortices (Figure S4C). The 19S complex recognizes ubiquitinated proteins, then deubiquitinates, unfolds, and translocates them to the 20S catalytic complex for degradation. The elevation of 19S molecules along with the tendency of increasing 20S activities in Brap^{cKONPC} mice suggested a compensatory attempt of the mutant to combat the increased UPS burden. Besides increased ubiquitination of canonical H2A, the abundance of multiple histone H2A variants, including H2A.X, H2A.Y, H2A.Z, H2A.W, and H2A.2B, was also significantly higher in Brap^{cKONPC} than in control cortices (Figure 7F). The significant changes in H2Aub and multiple histone H2A variants reflect the substantial chromatin remodeling in the Brap^{cKONPC} brain. They also support the notion that alterations of histone H2A and H2A variants can promote aging and neurodegeneration.

The overlapping transcriptomic and proteomic alterations between Brap^{cKONPC} mice and NDs prompted us to determine whether the brain defect caused by Brap LOF may underlie human brain aging and neurodegeneration, as there is an urgent need for animal models to uncover the origin and recapitulate the progression of NDs. To test whether our findings were applicable to human conditions, we examined postmortem brain samples of seven AD patients along with five age-matched normal controls (Table S3: Human Brain Tissue Table) to study their histone levels and histone H2A ubiquitination states. Considering the heterogeneity among the human postmortem specimens, differences in their protein solubility, and technical variation in histone extraction and IB detections, we looked at the levels of both mono- and multi/poly-histone H2A ubiquitination with pan-H2A antibodies and an antibody for H2AubK119. Our

analysis of the human tissue samples demonstrated that, compared with histone H2A, H2B, H3, H4, or H1, the level of combined mono- and penta-ubiquitinated H2A (H2Aub1+H2Aub5) was significantly higher in the cortical tissue of the AD group than in that of the control group (Figures 7G, 7H, and S4D). Besides an overall increase in ubiquitinated H2A shown by pan-H2A antibodies, a significant increase in the immunoreactivity of the H2AubK119 antibody was also found in AD relative to control brains. Similar to our observations of Brap^{cKO} mice, the elevation of histone H2Aub in the AD brains was not associated with a decrease in 20S proteasome activity (Figure S4E). The close resemblance in histone ubiquitination states between AD and Brap^{cKO} mice supports the relevance of our data to human NDs. It also suggests that H2Aub is a common epigenetic modification associated with brain aging and neurodegeneration, and that the Brap^{cKO} mouse model can be useful for studying AD and NDs.

DISCUSSION

In this study, we show that Brap LOF causes accelerated aging at the cellular, tissue, and organismal levels, resulting in significant lifespan shortening in mice. This finding is consistent with the results of recent large-scale GWAS that identified the association of the *BRAP* locus with human lifespan. They together suggest that a better understanding of *BRAP*'s gain and loss of function would provide insight into the molecular determinants for aging and longevity. Moreover, our studies of the cerebral cortical NPC- and neuron-specific Brap conditional knockout mice reveal a histone H2Aub-based mechanism that connects multiple aging hallmarks to neurodegeneration, serving as a new model for aging-associated diseases.

The interconnection of multiple aging hallmarks underpins the complex etiology of aging-associated diseases

Aging is an inevitable natural process driven by numerous molecular and cellular events that act synergistically to cause an irreversible functional decline of the organs involved. Through the model of Brap LOF, we have learned that the abnormal increase in histone H2Aub can serve as a nexus for multiple aging accelerating mechanisms. Histone H2A mono-ubiquitination has been implicated as an evolutionarily conserved aging biomarker from an ubiquitylome study of long-lived *Drosophila* proteins. It was shown to increase in an age-dependent manner not only in *Drosophila* but also in the brain of mice, non-human primates, and humans (Yang et al., 2019). Our data now echo this study, and we further demonstrate that the gained H2Aub in the aged Brap^{cKO} mouse and AD brains may include both mono and multi/poly ubiquitin modification that could occur at multiple sites of histone H2A and H2A variants. Moreover, we show that mono-H2Aub can progress to poly-H2Aub and promote UPS-mediated H2A degradation. Such histone proteolysis not only changes chromatin structure but also increases the UPS burden, leading to proteopathy and an irreversible senescent state in cells being affected.

Increased ubiquitination of histone H2A in Brap mutants appears to occur predominantly at the C-terminus on sites modified by Brca1 and/or PRC1, which induces ubiquitin-mediated H2A degradation and nucleosome destabilization. In histone octamers, H2A sits on the edges with the flexible C-terminus tail protruding from the globular nucleosome particle at the DNA entry/exit site. This structure makes the C-terminus of H2A spatially permissive to accommodate the bulky multi- or poly-ubiquitination. The histone H2A family contains numerous isoforms and variants, among which the highest degree of diversification is in their C-termini. It is intriguing that many histone H2A variants were increased along with H2Aub in the aging Brap^{cKONPC} brain. This could reflect the compensation for the loss of canonical H2A or alterations in the turnover of H2A variants, but the end result is a global chromatin structure change. Additional insights on the altered nucleosome structure as well as on the genomic loci involved in these H2A modifications and variants will allow a better understanding the chromatin state that drives senescence and aging.

It is especially intriguing that the overall level of H2Aub is increased in the cortical tissue of AD. Although the terminal brain pathology of AD is characterized by the accumulation of amyloid-β and hyperphosphorylated tau proteins, the cause of idiopathic AD remains elusive, though aging is known as the major risk factor. Our finding here suggests that histone H2Aub is a potential biomarker for AD, as the level of H2Aub may mark cells' or organs' pathophysiological age instead of chronological age by connecting chromatin aberration to cellular senescence and proteinopathy. Whereas H2Aub-mediated epigenetic and proteomic changes cause profound cell-intrinsic phenotypes, the senescence-associated autocrine and paracrine signaling can induce tissue-wide changes and immune-activation, leading to brain deterioration at multiple levels. Therefore, epigenetic aging may underlie NDs and other aging-associated diseases.

BRAP modulates BRCA1's cytoplasmic-nuclear shuttling in a context-dependent manner

BRAP/Brap is a multifunctional protein cloned originally through its ability to bind the nuclear localization signal (NLS) of the BRCA1 tumor suppressor and retain BRCA1 in the cytoplasm (Li et al., 1998). BRAP is also shown to act as a Ras-responsive ubiquitin E3 ligase that undergoes auto-ubiquitination to limit the activation of MAP kinase cascade (Matheny et al., 2004). In the developing CNS, Brap regulates MAPK signaling differentially according to the spatial position of NPCs (Lanctot et al., 2013). Brap E3 ligase can also regulate the turnover of other E3 ligases that modify many nuclear proteins (Lanctot et al., 2017). These make BRAP a versatile, yet powerful, molecule capable of connecting incoming signals that cells receive to cells' functional outputs governed by chromatin states.

Our data now suggest BRAP act between Ras and BRCA1 and can subsequently regulate BRCA1's cytoplasmic-nucleus shuttling based on cell type and cell state. Variations in BRCA1's nuclear vs cytoplasmic localization have a strong correlation with aggressive tumor features and prognosis (Chen et al., 1995; Scully et al., 1996; Wilson et al., 1999), though the function of cytoplasmic BRCA1 remains elusive. Brap LOF appears to create a condition in which Brca1's cytoplasmic pool is reduced, whereas Brca1's nuclear pool dominates in the context of sustained genome instability. In this condition, the higher levels of nuclear Brca1 and histone H2Aub are associated with impeded neurogenesis, cellular senescence, and accelerated aging. Notably, cellular senescence and impaired neural stem/progenitor cell function are also phenotypes of Brca1 null mutation and conditional deletion in neural progenitors, respectively (Cao et al., 2003; Pulvers and Huttner, 2009). Therefore, the shared phenotype between cells with full Brca1 absence and cells with low cytoplasmic-high nuclear Brca1 owing to Brap deficiency suggests that the cytoplasmic pool of Brca1 may be essential for maintaining stem cell function and suppressing senescence. Besides a major function in DSB repair, the ubiquitin E3 ligase activity is an integral element of nuclear BRCA1 in tumor suppression (Reid et al., 2008; Wu et al., 2008; Zhu et al., 2011). The high nuclear Brca1 in $Brap^{-/-}$ and $Brap^{cKO}$ cells is associated with sustained DSBs, increased H2Aub, and accelerated senescence. This raises a possibility that the BRCA1 E3 ligase may contribute to tumor suppression by directing cells with irreparable DSBs to senescence, though this would be at the expense of exhausting stem cells and speeding up the aging of those cells or organs with increased genome instability as seen in the Brap LOF model. Therefore, as a cytoplasmic docking protein, BRAP's regulation of BRCA1 could be dependent on the level of BRAP in a context-dependent manner: in stem and healthy somatic cells with high levels of BRAP, the cytoplasmic BRAC1 is maintained for cell proliferation, differentiation, and survival, whereas in cells with constitutive Ras activation or severe genomic lesions, the level of BRAP decreases by auto-ubiquitination and nuclear BRCA1 increases, promoting either DNA repair or H2Aub-mediated senescence. However, further studies of the physiological and pathological conditions by which BRAP differentially controls BRCA1's nuclear and cytoplasmic homeostasis remain necessary to delineate the diverse roles of BRCA1 in development, aging, and oncogenesis.

The senescent states are diverse and can apply to cortical neurons

Cellular senescence, defined traditionally as a cell that can no longer divide, is essentially a stress response to reactive oxygen species, DNA damage, and protein misfolding or aggregation. However, cellular senescence presents many acquired characteristics beyond cell cycle arrests, such as chromatin remodeling, metabolic activation, and SASP. Although NPCs and MEFs with Brap deficiency undergo canonical cellular senescence in culture, the senescent phenotype in cortical tissues of $Brap^{cKO}$ mice is more complex. Despite increases in bona fide senescence markers of SA-β-Gal and $p16^{Ink4a}$, there was no replication arrest of any type of brain-resident cells in the cerebral cortex of $Brap^{cKONPC}$ mice. Because the age-dependent neuroinflammation, proteopathy, brain structural deterioration, and midlife mortality were linked to Brap LOF in neurons showing DSBs, it suggests that cellular senescence is dictated by the chromatin state. Such chromatin state not only entails the permanent cessation of propagating cells with irreparable damage but also elicits a multitude of damage responses, leading to the widespread transcriptome, metabolome, and proteome alterations for cells to adjust their microenvironment and their interaction with neighboring cells. Therefore, cellular senescence might be better defined by the distinctive chromatin state, metabolic pattern, and SASP than by cell-cycle arrest alone. By this definition, neurons, which are intrinsically postmitotic, can further progress to a senescent state if they harbor sustained DSBs, leading to brain-wide metabolic and inflammatory changes.

Our RNA-seq with bulk cortical tissue identified 373 upregulated genes in $Brap^{cKONPC}$ mice, of which 80 encode secreted proteins. Whereas some of these transcripts could be from activated astrocytes, microglia, and lymphocytes, many are expected to represent primary SASP of Brap-deficient cortical neurons

with newly adopted epigenetic states. As the molecular responses of cellular senescence are context-dependent, the molecular composition of SASP is expected to be heterogeneous and pleiotropic, which can be both protective and destructive depending on the stage of phenotype progression. Further studies to identify primary SASP molecules from Brap-deficient cortical neurons in young and aged mice, respectively, will provide in-depth information on the initiation and progression of neuroinflammation and degeneration.

Intrinsic sources of genome instability in cerebral cortical neurons

DNA damage, particularly DSBs, have been shown to increase in the brains of AD, PD, and ALS patients (Kim et al., 2020; Mitra et al., 2019; Schaser et al., 2019; Shanbhag et al., 2019). Whereas genomic instability is considered a contributor to the pathogenesis of NDs, the causes of neuronal DSBs and the mechanism by which DSBs induce the degenerative brain pathology remain to be defined. In the cerebral cortical tissue, Brap LOF resulted in chronic DSBs specifically in neurons. Whereas this may be owing to neurons' high metabolic rate, potent generation of reactive oxygen species, and abundant polyunsaturated fatty acids prone to peroxidation, our data demonstrate that aberrant chromatin remodeling in neuronal differentiation could also lead to DSBs (Chomiak et al., 2021). During cortical neurogenesis, Brap acts synergistically with Nde1 to facilitate the compaction and epigenetic repression of constitutive heterochromatin composed of long tandem repetitive satellite DNA sequences. Brap LOF impairs constitutive heterochromatin remodeling and results in not only DSBs but also de-silencing of satellite DNA transcription and nuclear architecture aberrations in cortical neurons (Chomiak et al., 2021). Because of the repetitive nature of satellite DNA, damages to these elements tend to perpetuate and are refractory to repair. As neurons lack the ability of regeneration, the aberrant protection to constitutive heterochromatin is likely the main source of vulnerability to genotoxic insults throughout neurons' lifespan. Notably, chromatin immunoprecipitation (ChIP) analyses have shown that BRCA1-mediated mono-H2Aub is enriched in the satellite regions of the genome (Padeken et al., 2019; Zhu et al., 2011). Therefore, the persistently high level of histone H2Aub seen in Brap^{cKONPC} mice may not only mark the damaged loci but also alter the structure of constitutive heterochromatin. Consequently, the broad change in chromatin state can alter gene expression and metabolism to drive neurodegeneration.

The deep chromatin root of NDs and AD

Various NDs share common defects in the accumulation and aggregation of misfolded proteins despite the fact that each of them presents unique pathological hallmarks, specific brain regional involvement, and distinctive clinical symptoms. Tremendous effort has been made to target protein aggregates, especially the amyloid plaques in AD, but the efficacy of these treatment regimens has been uncertain, suggesting that the aggregated proteins are the terminally pathological manifestations rather than the original cause of neurodegeneration. It is currently believed that AD, and many other NDs, may have a long asymptomatic or prodromal phase that lasts as long as decades, during which the diseases are frequently associated with chronic neuroinflammation and brain vascular dysfunction. The complex etiology of NDs has also made it difficult to establish proper animal models. None of the existing models of AD, PD, or ALS fully phenocopy the human disease conditions and progression. It is thus extremely challenging to identify the early diagnostic markers as well as the initial cellular and molecular defect that primes the progressive brain tissue-wide deterioration.

We believe the Brap^{cKO} mouse model will be invaluable for understanding the molecular mechanism and early-phase pathogenesis of NDs and AD. The wide range of phenotypes presented by the Brap^{cKO} mice is well in line with the disease states of human NDs. Its molecular profiles of neuroinflammation as well as gene expression and proteomic aberrations overlap substantially with hallmark pathologies of AD, PD, HD, and ALS. Therefore, data obtained from Brap^{cKO} mice are justified to serve as entry points for exploring the deep roots and complex etiology of neurodegeneration. As suggested, there is a chromatin origin of AD and NDs. Given that dynamic chromatin remodeling is an intrinsic need for neuronal plasticity, genome instability, and epigenome aberrations are expected to have a constant and lifelong impact on neuronal function and longevity. A better understanding of chromatin quality control holds promises for the identification of early and effective targets and therapeutic intervention for NDs.

Limitations of the study

The study is based on phenotype analyses of Brap LOF in mice. Brap is an essential gene for mammalian development. It plays multifaceted roles in Ras signaling, cell cycle, ubiquitin-mediated protein turnover,

and nuclear import. Although increased histone H2Aub is a hallmark phenotype of Brap LOF, H2Aub is not a direct catalytic product of Brap, and the E3 ligase(s) that links Brap and H2Aub is not fully defined. Whereas Brca1 is likely one of the main players, molecules of the PRC1 complex are also likely to be downstream of Brap. The site-specific regulation of H2Aub by Brap is limited by the availability of site-specific antibodies against histone H2A and the complexity of the brain tissue.

DISCLAIMER

The opinions, interpretations, conclusions, and recommendation are those of the authors and are not necessarily endorsed by the U.S. Army, Department of Defense, the U.S. Government or the Uniformed Services University of the Health Sciences. The use of trade names does not constitute an official endorsement or approval of the use of reagents or commercial hardware or software. This document may not be cited for purposes of advertisement.

STAR★METHODS

Detailed methods are provided in the online version of this paper and include the following:

- KEY RESOURCE TABLE
- RESOURCE AVAILABILITY
  - Lead contact
  - Material availability
  - Data and code availability
- EXPERIMENTAL MODEL AND SUBJECT DETAILS
  - Mice
  - Human postmortem cerebral cortical tissue samples
- METHOD DETAILS
  - Cell culture
  - Immunoblotting
  - Immunostaining, immunofluorescence, and immunohistological analyses
  - Senescence-associated β-gal (SA-β-gal) staining
  - Golgi-Cox staining and dendritic spine analysis
  - Histone extractions
  - Cytoplasmic-nuclear fractionation
  - RNA isolation and quantitative RT-PCR
  - RNA sequencing analysis of whole cerebral cortical transcriptome
  - 10-Plex tandem mass tags (TMT) proteomic analysis
  - 20S Proteasome assay
- QUANTIFICATION AND STATISTICAL ANALYSIS

SUPPLEMENTAL INFORMATION

Supplemental information can be found online at https://doi.org/10.1016/j.isci.2022.104519.

ACKNOWLEDGMENTS

The authors wish to thank Barrington Burnett of Uniformed Services University for communication and discussion; the Genomics Facility of University of Chicago for RNA library construction and NGS analysis; the Thermo Fisher Center for Multiplexed Proteomics at the Harvard Medical School for tandem mass tag proteomic analysis; and the Biomedical Instrumentation Center of Uniformed Services University for qRT-PCR analysis. This work was supported by startup funds of Northwestern University and USUHS to Y.F. The UCI ADRC is funded by NIH/NIA Grant P30AG066519.

AUTHOR CONTRIBUTIONS

Y.F. conceptualized the project, designed and performed the experiments, interpreted the results, and wrote the manuscript. Y.G. performed experiments; A.A.C. initiated the study and performed the experiments. Y.H. performed data analyses, C.C.L performed experiments, C.A.K. performed experiments, and H.P. performed experiments. W-C.C. and J.A. performed bioinformatics data processing and analysis. X.Z. assisted with experiments. E.S.M. provided brain pathology expertise and human postmortem brain specimens.

DECLARATION OF INTERESTS

The authors declare that they have no conflict of interest.

Received: October 5, 2021
Revised: April 6, 2022
Accepted: May 29, 2022
Published: July 15, 2022

REFERENCES

Abdouh, M., Chatoo, W., El Hajjar, J., David, J., Ferreira, J., and Bernier, G. (2012). Bmi1 is down-regulated in the aging brain and displays antioxidant and protective activities in neurons. PLoS One *7*, e31870. https://doi.org/10.1371/journal.pone.0031870.

Alkuraya, F.S., Cai, X., Emery, C., Mochida, G.H., Al-Dosari, M.S., Felie, J.M., Hill, R.S., Barry, B.J., Partlow, J.N., Gascon, G.G., et al. (2011). Human mutations in NDE1 cause extreme microcephaly with lissencephaly. Am. J. Hum. Genet. *88*, 536–547. https://doi.org/10.1016/j.ajhg.2011.04.003.

Aoshiba, K., Tsuji, T., Kameyama, S., Itoh, M., Semba, S., Yamaguchi, K., and Nakamura, H. (2013). Senescence-associated secretory phenotype in a mouse model of bleomycin-induced lung injury. Exp. Toxicol. Pathol. *65*, 1053–1062. https://doi.org/10.1016/j.etp.2013.04.001.

Augustinack, J.C., Schneider, A., Mandelkow, E.M., and Hyman, B.T. (2002). Specific tau phosphorylation sites correlate with severity of neuronal cytopathology in Alzheimer's disease. Acta Neuropathol. *103*, 26–35. https://doi.org/10.1007/s004010100423.

Bakircioglu, M., Carvalho, O.P., Khurshid, M., Cox, J.J., Tuysuz, B., Barak, T., Yilmaz, S., Caglayan, O., Dincer, A., Nicholas, A.K., et al. (2011). The essential role of centrosomal NDE1 in human cerebral cortex neurogenesis. Am. J. Hum. Genet. *88*, 523–535. https://doi.org/10.1016/j.ajhg.2011.03.019.

Bushman, D.M., Kaeser, G.E., Siddoway, B., Westra, J.W., Rivera, R.R., Rehen, S.K., Yung, Y.C., and Chun, J. (2015). Genomic mosaicism with increased amyloid precursor protein (APP) gene copy number in single neurons from sporadic Alzheimer's disease brains. Elife *4*, e05116. https://doi.org/10.7554/elife.05116.

Campisi, J., and Robert, L. (2014). Cell senescence: role in aging and age-related diseases. Interdiscipl. Top Gerontol. *39*, 45–61. https://doi.org/10.1159/000358899.

Cao, L., Li, W., Kim, S., Brodie, S.G., and Deng, C.X. (2003). Senescence, aging, and malignant transformation mediated by p53 in mice lacking the Brca1 full-length isoform. Genes Dev. *17*, 201–213. https://doi.org/10.1101/gad.1050003.

Capparelli, C., Chiavarina, B., Whitaker-Menezes, D., Pestell, T.G., Pestell, R.G., Hulit, J., Andò, S., Howell, A., Martinez-Outschoorn, U.E., Sotgia, F., et al. (2012). CDK inhibitors (p16/p19/p21) induce senescence and autophagy in cancer-associated fibroblasts, "fueling" tumor growth via paracrine interactions, without an increase in neo-angiogenesis. Cell Cycle *11*, 3599–3610. https://doi.org/10.4161/cc.21884.

Castello, L.M., Raineri, D., Salmi, L., Clemente, N., Vaschetto, R., Quaglia, M., Garzaro, M., Gentilli, S., Navalesi, P., Cantaluppi, V., et al. (2017). Osteopontin at the crossroads of inflammation and tumor progression. Mediat. Inflamm. *2017*, 4049098. https://doi.org/10.1155/2017/4049098.

Chen, Y., Chen, C.F., Riley, D.J., Allred, D.C., Chen, P.L., Von Hoff, D., Osborne, C.K., and Lee, W.H. (1995). Aberrant subcellular localization of BRCA1 in breast cancer. Science *270*, 789–791. https://doi.org/10.1126/science.270.5237.789.

Chomiak, A.A., Lowe, C.C., Guo, Y., McDaniel, D., Pan, H., Zhou, X., Zhou, Q., Doughty, M.L., and Feng, Y. (2021). Nde1 is required for heterochromatin compaction and stability in neocortical neurons. Preprint at bioRxiv. https://doi.org/10.1101/2021.06.25.449848.

Choy, K.R., and Watters, D.J. (2018). Neurodegeneration in ataxia-telangiectasia: multiple roles of ATM kinase in cellular homeostasis. Dev. Dyn. *247*, 33–46. https://doi.org/10.1002/dvdy.24522.

Coppe, J.P., Desprez, P.Y., Krtolica, A., and Campisi, J. (2010). The senescence-associated secretory phenotype: the dark side of tumor suppression. Annu. Rev. Pathol. *5*, 99–118. https://doi.org/10.1146/annurev-pathol-121808-102144.

Coppe, J.P., Patil, C.K., Rodier, F., Sun, Y., Muñoz, D.P., Goldstein, J., Nelson, P.S., Desprez, P.Y., and Campisi, J. (2008). Senescence-associated secretory phenotypes reveal cell-nonautonomous functions of oncogenic RAS and the p53 tumor suppressor. PLoS Biol. *6*, e301. https://doi.org/10.1371/journal.pbio.0060301.

Coppede, F., and Migliore, L. (2010). DNA repair in premature aging disorders and neurodegeneration. Curr. Aging Sci. *3*, 3–19. https://doi.org/10.2174/1874609811003010003.

Dewachter, I., Reversé, D., Caluwaerts, N., Ris, L., Kuipéri, C., Van den Haute, C., Spittaels, K., Umans, L., Serneels, L., Thiry, E., et al. (2002). Neuronal deficiency of presenilin 1 inhibits amyloid plaque formation and corrects hippocampal long-term potentiation but not a cognitive defect of amyloid precursor protein [V717I] transgenic mice. J. Neurosci. *22*, 3445–3453. https://doi.org/10.1523/jneurosci.22-09-03445.2002.

Dou, Z., Xu, C., Donahue, G., Shimi, T., Pan, J.A., Zhu, J., Ivanov, A., Capell, B.C., Drake, A.M., Shah, P.P., et al. (2015). Autophagy mediates degradation of nuclear lamina. Nature *527*, 105–109. https://doi.org/10.1038/nature15548.

El Hajjar, J., Chatoo, W., Hanna, R., Nkanza, P., Tétreault, N., Tse, Y.C., Wong, T.P., Abdouh, M., and Bernier, G. (2019). Heterochromatic genome instability and neurodegeneration sharing similarities with Alzheimer's disease in old Bmi1+/- mice. Sci. Rep. *9*, 594. https://doi.org/10.1038/s41598-018-37444-3.

Feser, J., Truong, D., Das, C., Carson, J.J., Kieft, J., Harkness, T., and Tyler, J.K. (2010). Elevated histone expression promotes life span extension. Mol. Cell *39*, 724–735. https://doi.org/10.1016/j.molcel.2010.08.015.

Flanagan, K.C., Alspach, E., Pazolli, E., Parajuli, S., Ren, Q., Arthur, L.L., Tapia, R., and Stewart, S.A. (2018). c-Myb and C/EBPβ regulate OPN and other senescence-associated secretory phenotype factors. Oncotarget *9*, 21–36. https://doi.org/10.18632/oncotarget.22940.

Freund, A., Orjalo, A.V., Desprez, P.Y., and Campisi, J. (2010). Inflammatory networks during cellular senescence: causes and consequences. Trends Mol. Med. *16*, 238–246. https://doi.org/10.1016/j.molmed.2010.03.003.

Frost, G.R., Jonas, L.A., and Li, Y.M. (2019). Friend, foe or both? Immune activity in Alzheimer's disease. Front. Aging Neurosci. *11*, 337. https://doi.org/10.3389/fnagi.2019.00337.

Ghosh, K., and Capell, B.C. (2016). The senescence-associated secretory phenotype: critical effector in skin cancer and aging. J. Invest. Dermatol. *136*, 2133–2139. https://doi.org/10.1016/j.jid.2016.06.621.

Gorski, J.A., Talley, T., Qiu, M., Puelles, L., Rubenstein, J.L.R., and Jones, K.R. (2002). Cortical excitatory neurons and glia, but not GABAergic neurons, are produced in the Emx1-expressing lineage. J. Neurosci. *22*, 6309–6314. https://doi.org/10.1523/jneurosci.22-15-06309.2002.

Haber, D.A. (1997). Splicing into senescence: the curious case of p16 and p19ARF. Cell *91*, 555–558. https://doi.org/10.1016/s0092-8674(00)80441-9.

Hayflick, L. (1965). The limited in vitro lifetime of human diploid cell strains. Exp. Cell Res. *37*, 614–636. https://doi.org/10.1016/0014-4827(65)90211-9.

Hernandez-Segura, A., Nehme, J., and Demaria, M. (2018). Hallmarks of cellular senescence. Trends Cell Biol. *28*, 436–453. https://doi.org/10.1016/j.tcb.2018.02.001.

Hoang, M.L., Kinde, I., Tomasetti, C., McMahon, K.W., Rosenquist, T.A., Grollman, A.P., Kinzler, K.W., Vogelstein, B., and Papadopoulos, N. (2016). Genome-wide quantification of rare somatic mutations in normal human tissues using massively parallel sequencing. Proc. Natl. Acad.

Sci. U S A *113*, 9846–9851. https://doi.org/10.1073/pnas.1607794113.

Horn, V., Uckelmann, M., Zhang, H., Eerland, J., Aarsman, I., le Paige, U.B., Davidovich, C., Sixma, T.K., and van Ingen, H. (2019). Structural basis of specific H2A K13/K15 ubiquitination by RNF168. Nat. Commun. *10*, 1751. https://doi.org/10.1038/s41467-019-09756-z.

Houlihan, S.L., and Feng, Y. (2014). The scaffold protein Nde1 safeguards the brain genome during S phase of early neural progenitor differentiation. Elife *3*, e03297. https://doi.org/10.7554/elife.03297.

Hu, Z., Chen, K., Xia, Z., Chavez, M., Pal, S., Seol, J.H., Chen, C.C., Li, W., and Tyler, J.K. (2014). Nucleosome loss leads to global transcriptional up-regulation and genomic instability during yeast aging. Genes Dev. *28*, 396–408. https://doi.org/10.1101/gad.233221.113.

Ivanov, A., Pawlikowski, J., Manoharan, I., van Tuyn, J., Nelson, D.M., Rai, T.S., Shah, P.P., Hewitt, G., Korolchuk, V.I., Passos, J.F., et al. (2013). Lysosome-mediated processing of chromatin in senescence. J. Cell Biol. *202*, 129–143. https://doi.org/10.1083/jcb.201212110.

Jicha, G.A., Lane, E., Vincent, I., Otvos, L., Jr., Hoffmann, R., and Davies, P. (1997). A conformation- and phosphorylation-dependent antibody recognizing the paired helical filaments of Alzheimer's disease. J. Neurochem. *69*, 2087–2095. https://doi.org/10.1046/j.1471-4159.1997.69052087.x.

Jullien, J., Vodnala, M., Pasque, V., Oikawa, M., Miyamoto, K., Allen, G., David, S.A., Brochard, V., Wang, S., Bradshaw, C., et al. (2017). Gene resistance to transcriptional reprogramming following nuclear transfer is directly mediated by multiple chromatin-repressive pathways. Mol. Cell *65*, 873–884.e8. https://doi.org/10.1016/j.molcel.2017.01.030.

Kakigi, R., Endo, C., Neshige, R., Kohno, H., and Kuroda, Y. (1992). Accelerated aging of the brain in Werner's syndrome. Neurology *42*, 922. https://doi.org/10.1212/wnl.42.4.922.

Kalb, R., Mallery, D.L., Larkin, C., Huang, J.T., and Hiom, K. (2014). BRCA1 is a histone-H2A-specific ubiquitin ligase. Cell Rep. *8*, 999–1005. https://doi.org/10.1016/j.celrep.2014.07.025.

Kim, B.J., Chan, D.W., Jung, S.Y., Chen, Y., Qin, J., and Wang, Y. (2017). The histone variant MacroH2A1 is a BRCA1 ubiquitin ligase substrate. Cell Rep. *19*, 1758–1766. https://doi.org/10.1016/j.celrep.2017.05.027.

Kim, B.W., Jeong, Y.E., Wong, M., and Martin, L.J. (2020). DNA damage accumulates and responses are engaged in human ALS brain and spinal motor neurons and DNA repair is activatable in iPSC-derived motor neurons with SOD1 mutations. Acta Neuropathol. Commun. *8*, 7. https://doi.org/10.1186/s40478-019-0874-4.

Kuilman, T., and Peeper, D.S. (2009). Senescence-messaging secretome: SMS-ing cellular stress. Nat. Rev. Cancer *9*, 81–94. https://doi.org/10.1038/nrc2560.

Lanctot, A.A., Guo, Y., Le, Y., Edens, B.M., Nowakowski, R.S., and Feng, Y. (2017). Loss of Brap results in premature G1/S phase transition and impeded neural progenitor differentiation. Cell Rep. *20*, 1148–1160. https://doi.org/10.1016/j.celrep.2017.07.018.

Lanctot, A.A., Peng, C.Y., Pawlisz, A.S., Joksimovic, M., and Feng, Y. (2013). Spatially dependent dynamic MAPK modulation by the Nde1-Lis1-Brap complex patterns mammalian CNS. Dev. Cell *25*, 241–255. https://doi.org/10.1016/j.devcel.2013.04.006.

Lasry, A., and Ben-Neriah, Y. (2015). Senescence-associated inflammatory responses: aging and cancer perspectives. Trends Immunol. *36*, 217–228. https://doi.org/10.1016/j.it.2015.02.009.

Li, S., Ku, C.Y., Farmer, A.A., Cong, Y.S., Chen, C.F., and Lee, W.H. (1998). Identification of a novel cytoplasmic protein that specifically binds to nuclear localization signal motifs. J. Biol. Chem. *273*, 6183–6189. https://doi.org/10.1074/jbc.273.11.6183.

Liu, K., Ding, L., Li, Y., Yang, H., Zhao, C., Lei, Y., Han, S., Tao, W., Miao, D., Steller, H., et al. (2014). Neuronal necrosis is regulated by a conserved chromatin-modifying cascade. Proc. Natl. Acad. Sci. U S A *111*, 13960–13965. https://doi.org/10.1073/pnas.1413644111.

Lodato, M.A., Rodin, R.E., Bohrson, C.L., Coulter, M.E., Barton, A.R., Kwon, M., Sherman, M.A., Vitzthum, C.M., Luquette, L.J., Yandava, C.N., et al. (2018). Aging and neurodegeneration are associated with increased mutations in single human neurons. Science *359*, 555–559. https://doi.org/10.1126/science.aao4426.

Lodato, M.A., Woodworth, M.B., Lee, S., Evrony, G.D., Mehta, B.K., Karger, A., Lee, S., Chittenden, T.W., D'Gama, A.M., Cai, X., et al. (2015). Somatic mutation in single human neurons tracks developmental and transcriptional history. Science *350*, 94–98. https://doi.org/10.1126/science.aab1785.

Lombard, D.B., Chua, K.F., Mostoslavsky, R., Franco, S., Gostissa, M., and Alt, F.W. (2005). DNA repair, genome stability, and aging. Cell *120*, 497–512. https://doi.org/10.1016/j.cell.2005.01.028.

Lopez-Otin, C., Blasco, M.A., Partridge, L., Serrano, M., and Kroemer, G. (2013). The hallmarks of aging. Cell *153*, 1194–1217. https://doi.org/10.1016/j.cell.2013.05.039.

Lu, T., Pan, Y., Kao, S.Y., Li, C., Kohane, I., Chan, J., and Yankner, B.A. (2004). Gene regulation and DNA damage in the ageing human brain. Nature *429*, 883–891. https://doi.org/10.1038/nature02661.

Luczak, M.W., and Zhitkovich, A. (2018). Monoubiquitinated gamma-H2AX: abundant product and specific biomarker for non-apoptotic DNA double-strand breaks. Toxicol. Appl. Pharmacol. *355*, 238–246. https://doi.org/10.1016/j.taap.2018.07.007.

Madabhushi, R., Pan, L., and Tsai, L.H. (2014). DNA damage and its links to neurodegeneration. Neuron *83*, 266–282. https://doi.org/10.1016/j.neuron.2014.06.034.

Matheny, S.A., Chen, C., Kortum, R.L., Razidlo, G.L., Lewis, R.E., and White, M.A. (2004). Ras regulates assembly of mitogenic signalling complexes through the effector protein IMP. Nature *427*, 256–260. https://doi.org/10.1038/nature02237.

Mattiroli, F., and Penengo, L. (2021). Histone ubiquitination: an integrative signaling platform in genome stability. Trends Genet. *37*, 566–581. https://doi.org/10.1016/j.tig.2020.12.005.

Mattson, M.P., and Arumugam, T.V. (2018). Hallmarks of brain aging: adaptive and pathological modification by metabolic states. Cell Metab. *27*, 1176–1199. https://doi.org/10.1016/j.cmet.2018.05.011.

McHugh, D., and Gil, J. (2018). Senescence and aging: causes, consequences, and therapeutic avenues. J. Cell Biol. *217*, 65–77. https://doi.org/10.1083/jcb.201708092.

Mitra, J., Guerrero, E.N., Hegde, P.M., Liachko, N.F., Wang, H., Vasquez, V., Gao, J., Pandey, A., Taylor, J.P., Kraemer, B.C., et al. (2019). Motor neuron disease-associated loss of nuclear TDP-43 is linked to DNA double-strand break repair defects. Proc. Natl. Acad. Sci. U S A *116*, 4696–4705. https://doi.org/10.1073/pnas.1818415116.

Munoz-Espin, D., and Serrano, M. (2014). Cellular senescence: from physiology to pathology. Nat. Rev. Mol. Cell Biol. *15*, 482–496. https://doi.org/10.1038/nrm3823.

Musi, N., Valentine, J.M., Sickora, K.R., Baeuerle, E., Thompson, C.S., Shen, Q., and Orr, M.E. (2018). Tau protein aggregation is associated with cellular senescence in the brain. Aging Cell *17*, e12840. https://doi.org/10.1111/acel.12840.

Newcombe, E.A., Camats-Perna, J., Silva, M.L., Valmas, N., Huat, T.J., and Medeiros, R. (2018). Inflammation: the link between comorbidities, genetics, and Alzheimer's disease. J. Neuroinflammation *15*, 276. https://doi.org/10.1186/s12974-018-1313-3.

Padeken, J., Zeller, P., Towbin, B., Katic, I., Kalck, V., Methot, S.P., and Gasser, S.M. (2019). Synergistic lethality between BRCA1 and H3K9me2 loss reflects satellite derepression. Genes Dev. *33*, 436–451. https://doi.org/10.1101/gad.322495.118.

Panier, S., and Boulton, S.J. (2014). Double-strand break repair: 53BP1 comes into focus. Nat. Rev. Mol. Cell Biol. *15*, 7–18. https://doi.org/10.1038/nrm3719.

Pazolli, E., Alspach, E., Milczarek, A., Prior, J., Piwnica-Worms, D., and Stewart, S.A. (2012). Chromatin remodeling underlies the senescence-associated secretory phenotype of tumor stromal fibroblasts that supports cancer progression. Cancer Res. *72*, 2251–2261. https://doi.org/10.1158/0008-5472.can-11-3386.

Pulvers, J.N., and Huttner, W.B. (2009). Brca1 is required for embryonic development of the mouse cerebral cortex to normal size by preventing apoptosis of early neural progenitors. Development *136*, 1859–1868. https://doi.org/10.1242/dev.033498.

Quelle, D.E., Zindy, F., Ashmun, R.A., and Sherr, C.J. (1995). Alternative reading frames of the INK4a tumor suppressor gene encode two unrelated proteins capable of inducing cell cycle arrest. Cell *83*, 993–1000. https://doi.org/10.1016/0092-8674(95)90214-7.

Rao, S.G., and Jackson, J.G. (2016). SASP: tumor suppressor or promoter? Yes! Trends Cancer *2*, 676–687. https://doi.org/10.1016/j.trecan.2016.10.001.

Reid, L.J., Shakya, R., Modi, A.P., Lokshin, M., Cheng, J.T., Jasin, M., Baer, R., and Ludwig, T. (2008). E3 ligase activity of BRCA1 is not essential for mammalian cell viability or homology-directed repair of double-strand DNA breaks. Proc. Natl. Acad. Sci. U S A *105*, 20876–20881. https://doi.org/10.1073/pnas.0811203106.

Rodier, F., and Campisi, J. (2011). Four faces of cellular senescence. J. Cell Biol. *192*, 547–556. https://doi.org/10.1083/jcb.201009094.

Rulten, S.L., and Caldecott, K.W. (2013). DNA strand break repair and neurodegeneration. DNA Repair *12*, 558–567. https://doi.org/10.1016/j.dnarep.2013.04.008.

Rutten, B.P., Schmitz, C., Gerlach, O.H., Oyen, H.M., de Mesquita, E.B., Steinbusch, H.W., and Korr, H. (2007). The aging brain: accumulation of DNA damage or neuron loss? Neurobiol. Aging *28*, 91–98. https://doi.org/10.1016/j.neurobiolaging.2005.10.019.

Salminen, A., Kauppinen, A., and Kaarniranta, K. (2012). Emerging role of NF-κB signaling in the induction of senescence-associated secretory phenotype (SASP). Cell. Signal. *24*, 835–845. https://doi.org/10.1016/j.cellsig.2011.12.006.

Sarlus, H., and Heneka, M.T. (2017). Microglia in Alzheimer's disease. J. Clin. Invest. *127*, 3240–3249. https://doi.org/10.1172/jci90606.

Schaser, A.J., Osterberg, V.R., Dent, S.E., Stackhouse, T.L., Wakeham, C.M., Boutros, S.W., Weston, L.J., Owen, N., Weissman, T.A., Luna, E., et al. (2019). Alpha-synuclein is a DNA binding protein that modulates DNA repair with implications for Lewy body disorders. Sci. Rep. *9*, 10919. https://doi.org/10.1038/s41598-019-47227-z.

Scully, R., Ganesan, S., Brown, M., De Caprio, J.A., Cannistra, S.A., Feunteun, J., Schnitt, S., and Livingston, D.M. (1996). Location of BRCA1 in human breast and ovarian cancer cells. Science *272*, 123–125. https://doi.org/10.1126/science.272.5258.123.

Shanbhag, N.M., Evans, M.D., Mao, W., Nana, A.L., Seeley, W.W., Adame, A., Rissman, R.A., Masliah, E., and Mucke, L. (2019). Early neuronal accumulation of DNA double strand breaks in Alzheimer's disease. Acta Neuropathol. Commun. *7*, 77. https://doi.org/10.1186/s40478-019-0723-5.

Soares, J.P., Cortinhas, A., Bento, T., Leitão, J.C., Collins, A.R., Gaivã, I., and Mota, M.P. (2014). Aging and DNA damage in humans: a meta-analysis study. Aging (Albany NY) *6*, 432–439. https://doi.org/10.18632/aging.100667.

Srivastava, A.K., Choudhury, S.R., and Karmakar, S. (2021). Neuronal Bmi-1 is critical for melatonin induced ubiquitination and proteasomal degradation of alpha-synuclein in experimental Parkinson's disease models. Neuropharmacology *194*, 108372. https://doi.org/10.1016/j.neuropharm.2020.108372.

Suarez-Calvet, M., Karikari, T.K., Ashton, N.J., Lantero Rodriguez, J., Mila-Aloma, M., Gispert, J.D., Salvado, G., Minguillon, C., Fauria, K., Shekari, M., et al. (2020). Novel tau biomarkers phosphorylated at T181, T217 or T231 rise in the initial stages of the preclinical Alzheimer's continuum when only subtle changes in Aβ pathology are detected. EMBO Mol. Med. *12*, e12921. https://doi.org/10.15252/emmm.202012921.

Suberbielle, E., Sanchez, P.E., Kravitz, A.V., Wang, X., Ho, K., Eilertson, K., Devidze, N., Kreitzer, A.C., and Mucke, L. (2013). Physiologic brain activity causes DNA double-strand breaks in neurons, with exacerbation by amyloid-β. Nat. Neurosci. *16*, 613–621. https://doi.org/10.1038/nn.3356.

Taherbhoy, A.M., Huang, O.W., and Cochran, A.G. (2015). BMI1-RING1B is an autoinhibited RING E3 ubiquitin ligase. Nat. Commun. *6*, 7621. https://doi.org/10.1038/ncomms8621.

Tamburri, S., Lavarone, E., Fernández-Pérez, D., Conway, E., Zanotti, M., Manganaro, D., and Pasini, D. (2020). Histone H2AK119 mono-ubiquitination is essential for polycomb-mediated transcriptional repression. Mol. Cell *77*, 840–856.e5. https://doi.org/10.1016/j.molcel.2019.11.021.

Thadathil, N., Hori, R., Xiao, J., and Khan, M.M. (2019). DNA double-strand breaks: a potential therapeutic target for neurodegenerative diseases. Chromosome Res. *27*, 345–364. https://doi.org/10.1007/s10577-019-09617-x.

Thiriet, C., and Hayes, J.J. (2005). Chromatin in need of a fix: phosphorylation of H2AX connects chromatin to DNA repair. Mol. Cell *18*, 617–622. https://doi.org/10.1016/j.molcel.2005.05.008.

Timmers, P.R., Mounier, N., Lall, K., Fischer, K., Ning, Z., Feng, X., Bretherick, A.D., Clark, D.W., eQTLGen Consortium, Agbessi, M., AHsan, H., et al. (2019). Genomics of 1 million parent lifespans implicates novel pathways and common diseases and distinguishes survival chances. Elife *8*, e39856. https://doi.org/10.7554/eLife.39856.

Todaro, G.J., and Green, H. (1963). Quantitative studies of the growth of mouse embryo cells in culture and their development into established lines. J. Cell Biol. *17*, 299–313. https://doi.org/10.1083/jcb.17.2.299.

Uckelmann, M., and Sixma, T.K. (2017). Histone ubiquitination in the DNA damage response. DNA Repair *56*, 92–101. https://doi.org/10.1016/j.dnarep.2017.06.011.

Vaughan, D.E., Rai, R., Khan, S.S., Eren, M., and Ghosh, A.K. (2017). Plasminogen activator inhibitor-1 is a marker and a mediator of senescence. Arterioscler. Thromb. Vasc. Biol. *37*, 1446–1452. https://doi.org/10.1161/atvbaha.117.309451.

Wang, H., Wang, L., Erdjument-Bromage, H., Vidal, M., Tempst, P., Jones, R.S., and Zhang, Y. (2004). Role of histone H2A ubiquitination in Polycomb silencing. Nature *431*, 873–878. https://doi.org/10.1038/nature02985.

Weidenheim, K.M., Dickson, D.W., and Rapin, I. (2009). Neuropathology of Cockayne syndrome: evidence for impaired development, premature aging, and neurodegeneration. Mech. Ageing Dev. *130*, 619–636. https://doi.org/10.1016/j.mad.2009.07.006.

White, R.R., and Vijg, J. (2016). Do DNA double-strand breaks drive aging? Mol. Cell *63*, 729–738. https://doi.org/10.1016/j.molcel.2016.08.004.

Wilson, C.A., Ramos, L., Villaseñor, M.R., Anders, K.H., Press, M.F., Clarke, K., Karlan, B., Chen, J.J., Scully, R., Livingston, D., et al. (1999). Localization of human BRCA1 and its loss in high-grade, non-inherited breast carcinomas. Nat. Genet. *21*, 236–240. https://doi.org/10.1038/6029.

Wu, J., Huen, M.S.Y., Lu, L.Y., Ye, L., Dou, Y., Ljungman, M., Chen, J., and Yu, X. (2009). Histone ubiquitination associates with BRCA1-dependent DNA damage response. Mol. Cell Biol. *29*, 849–860. https://doi.org/10.1128/mcb.01302-08.

Wu, W., Koike, A., Takeshita, T., and Ohta, T. (2008). The ubiquitin E3 ligase activity of BRCA1 and its biological functions. Cell Div. *3*, 1. https://doi.org/10.1186/1747-1028-3-1.

Yang, L., Ma, Z., Wang, H., Niu, K., Cao, Y., Sun, L., Geng, Y., Yang, B., Gao, F., Chen, Z., et al. (2019). Ubiquitylome study identifies increased histone 2A ubiquitylation as an evolutionarily conserved aging biomarker. Nat. Commun. *10*, 2191. https://doi.org/10.1038/s41467-019-10136-w.

Zhu, Q., Pao, G.M., Huynh, A.M., Suh, H., Tonnu, N., Nederlof, P.M., Gage, F.H., and Verma, I.M. (2011). BRCA1 tumour suppression occurs via heterochromatin-mediated silencing. Nature *477*, 179–184. https://doi.org/10.1038/nature10371.

STAR★METHODS

KEY RESOURCE TABLE

REAGENT or RESOURCE	SOURCE	IDENTIFIER
Antibodies		
Cyclin A	Santa Cruz Biotechnology	Cat# sc-751; RRID:AB_631329
P19 Arf	Novus Biologicals	Cat# NB200-169
p21 Cip1	Millipore	Cat# MAB88058; RRID:AB_11212534
p27 Kip1	Millipore	Cat# 06-445; RRID:AB_310121
p27 Kip (Clone DCS-72.F6)	ThermoFisher	Cat# MS-256-P0
p27Kip (F8)	Santa Cruz Biotechnology	Cat# sc-1641; RRID:AB_628074
NFkB p65	Cell Signaling Technology	Cat# 4764; RRID:AB_823578
phospho-NF-kB p65 (Ser365) (93H1)	Cell Signaling Technology	Cat# 3033; RRID:AB_331284
Cyclin A	Santa Cruz Biotechnology	Cat# sc-751; RRID:AB_631329
P19 Arf	Novus Biologicals	Cat# NB200-169
Ki67	Novo CASTRA	Cat# NCL-Ki67p
Ki67	eBioscience	Cat# 14-5698
Phospho-p53 (Ser15)	Abcam	Cat# ab1431; RRID:AB_301090
Phospho-p53 (Ser15) (D4S1H)	Cell Signaling Technology	Cat# 12571; RRID:AB_2714036
Phospho-p53 (Ser15) (16G8)	Cell Signaling Technology	Cat# 9286; RRID:AB_331741
Phospho-ATM(Ser1981)	Novus Biologicals	Cat# AF1655
Phospho-ATR (Ser 428)	Cell Signaling Technology	Cat# 2853; RRID:AB_2290281
53 BP1	Novus Biologicals	Cat# NB100-304
Brca1	Santa Cruz Biotechnology	Cat# sc-642; RRID:AB_630944
Brca1	Novus Biologicals	Cat# MAB22101
Brca1 (clone 8F7)	Novus Biologicals	Cat# NBP1-41186
LC3B (G-9)	Santa Cruz Biotechnology	Cat# sc-376404; RRID:AB_11150489
LC3B	Cell Signaling Technology	Cat# 2775; RRID:AB_915950
LC3B	Novus Biologicals	Cat# NB100-2220
p62SQSTM1	Novus Biologicals	Cat# MAB8028
p62SQSTM1	GeneTex	Cat# GTX100685; RRID:AB_2038029
Fibronectin	BD Biosciences	Cat# 610077; RRID:AB_2105706
Phospho-Tau (Thr181) 5H9L11	Thermo Fisher	Cat# 701530; RRID:AB_2532491
Phospho-Tau (Ser202/Thr205) mAb (AT8)	ThermoFisher	Cat# MN1020; RRID:AB_223647
Phospho-Tau (Thr231)	ThermoFisher	Cat# 44-746G; RRID:AB_2533742
Phospho-Tau (Ser416) D7U2P	Cell Signaling Technology	Cat# 15013; RRID:AB_2728782
Phospho-Tau (Thr 217)	GenScript	Cat# A00896; RRID:AB_2622113
Phospho-Tau (Ser396)	GenScript	Cat# A01387; RRID:AB_1575880
Tau (Tau 46)	Santa Cruz Biotechnology	Cat# sc32274; RRID:AB_628327
Tau (A10)	Santa Cruz Biotechnology	Cat# sc-390476
Tau (TAU-5)	Santa Cruz Biotechnology	Cat# sc-58860; RRID:AB_785931
Prp (6D11)	Santa Cruz Biotechnology	Cat# sc-58581; RRID:AB_1128724
Histone H1.0	Active Motif	Cat# 61417; RRID:AB_2793627
Histone H1	Active Motif	Cat# 39707; RRID:AB_2793314
Histone H1 (AE-4)	Santa Cruz Biotechnology	Cat# sc-8030; RRID:AB_675641
Histone H2A (D6O3A) Rabbit mAb	Cell Signaling Technology	Cat# 12349; RRID:AB_2687875

(*Continued on next page*)

Continued

REAGENT or RESOURCE	SOURCE	IDENTIFIER
Histone H2A II	Cell Signaling Technology	Cat# 2578; RRID:AB_2118804
Histone H2A, Clone C10037	MBL	Cat# D210-3
Histone H2A C-terminal antibody (pAb)	Active Motif	Cat# 39591; RRID:AB_2793270
Histone H2A	GeneTex	Cat# GTX129418; RRID:AB_2885986
Ubiquityl-Histone H2AK119	Cell Signaling Technology	Cat# 8240; RRID:AB_10891618
Ubiquityl-Histone H2A Clone E6C5	Millipore	Cat# 05-678; RRID:AB_11214408
Histone H2A.X	Active Motif	Cat# 39689; RRID:AB_2728764
Histone H2A.Z	Cell Signaling Technology	Cat# 2718; RRID:AB_659840
phospho-Histone H2A.X (Ser139), clone JBW301	Millipore	Cat# 05-636; RRID:AB_309864
phospho-Histone H2A.X (Ser139)	Cell Signaling Technology	Cat# 2577; RRID:AB_2118010
phapho-Histone H2A.X (Ser139)	Active Motif	Cat# 39117; RRID:AB_2793161
phospho-Histone H2A.X (Ser139)	Bethyl Laboratories	Cat# IHC-00059-3
phospho-Histone H2A.X (Ser139) Clone 2F3	Biolegend	Cat# 613401; RRID:AB_315794
H2A.Y/macroH2A.1	Cell Signaling Technology	Cat# 8551; RRID:AB_2797647
H2A.Y/macroH2A.1 Clone 866416	Novus Biologicals	Cat# MAB8318
Histone H2B	Active Motif	Cat# 39125; RRID:AB_2793163
Ubiquityl-Histone H2B K120	Active Motif	Cat# 39623; RRID:AB_2793279
Histone H3	Active Motif	Cat# 61799; RRID:AB_2793771
Histone H3K9me3	Abcam	Cat# ab8898; RRID:AB_306848
Histone H3 (1G1)	Epigentek	Cat# A68386
Histone H3	Cell Signaling Technology	Cat# 9715; RRID:AB_331563
Histone H3.3	Novus Biologicals	Cat# NBP2-24697
Histone H4	Active Motif	Cat# 39269; RRID:AB_2636967
Histone H4	GeneTex	Cat# GTX129560; RRID:AB_2886030
Lamin B1	Abcam	Cat# ab16048; RRID:AB_443298
Lamin B1 (M20)	Santa Cruz Biotechnology	Cat# sc-6217; RRID:AB_648158
Lamin A/C	Cell Signaling Technology	Cat# 4777; RRID:AB_10545756
Lamin A/C	BD Biosciences	Cat# 612162; RRID:AB_399533
Ring1B (D22F2)	Cell Signaling Technology	Cat# 5694; RRID:AB_10705604
RNF168	Santa Cruz Biotechnology	Cat# sc-101125
RNF168	Millipore	Cat# ABE367; RRID:AB_11205761
MMP1	GeneTex	Cat# GTX100534S; RRID:AB_10724220
MMP2	GeneTex	Cat# GTX104577; RRID:AB_1950932
MMP2	Proteintech	Cat# 66366-1; RRID:AB_2881746
OPN	Novus Biologicals	Cat# AF808
Pai1	Proteintech	Cat# 13801-1-AP; RRID:AB_2186881
CD68 (KP1)	Abcam	Cat# ab955; RRID:AB_307338
CD68 (FA-11)	Abcam	Cat# ab53444; RRID:AB_869007
Iba	Wako	Cat# 019-19741; RRID:AB_839504
GFAP	Abcam	Cat# ab7260; RRID:AB_305808
GFAP	Dako	Cat# GA52461-2
GFAP (GA5)	Novus Biologicals	Cat# NBP2-29415
NeuN	Cell Signaling Technology	Cat# 24307; RRID:AB_2651140
NeuN, Clone A60	Millipore	Cat# MAB377; RRID:AB_2298772

(*Continued on next page*)

Continued

REAGENT or RESOURCE	SOURCE	IDENTIFIER
Cleaved Caspase-3	Cell Signaling Technology	Cat# 9661; RRID:AB_2341188
Cleaved Caspase-3	Cell Signaling Technology	Cat# 9664; RRID:AB_2070042
Ubiquitin, Clone Ubi-1	Millipore	Cat# MAB1510; RRID:AB_2180556
Ubiquitin (Ubi-1)	Novus Biologicals	Cat# NB300-130
Ubiquitin	Millipore	Cat# AB1690; RRID:AB_2180744
Multiubiquitin Chain, Clone FK1	Cayman Chemical	Cat# 14219
Multiubiquitin Chain, Clone FK2	Cayman Chemical	Cat# 14220
Ubiqutin K48 linkage specific	Millipore	Cat# 05-1307; RRID:AB_1587578
Ubiqutin K63 linkage specific	Millipore	Cat# 05-1313; RRID:AB_1587585
Ubiqutin K11 linkage	Millipore	Cat# MABS107-I; RRID:AB_2713901
20S Proteasome alpha 2 (B4)	Santa Cruz Biotechnology	Cat# sc-377148
20S Proteasome beta 2 (D8)	Santa Cruz Biotechnology	Cat# sc-515066
Nucleoporin p62	BD Biosciences	Cat# 610497; RRID:AB_397863
Smc1	Novus Biologicals	Cat# NB100-204
GAPDH	Sigma	Cat# G9295; RRID:AB_1078992
Actin	Sigma	Cat# A2668; RRID:AB_258014
Tubulin, alpha, clone B-5-1-2	Sigma	Cat# T6074; RRID:AB_477582
Vinculin	Sigma	Cat# V9131; RRID:AB_477629
Biological samples		
Human postmortem cerebral cortical tissue samples		See Table S3: Human Postmortem AD and Control Brain Tissue Specimen Table.
Chemicals, peptides, and recombinant proteins		
Formaldehyde, EM grade	Ted Pella	Cat# 18505
Glutaraldehyde, EM grade	Ted Pella	Cat# 18421
X-Gal	ThermoFisher	Cat# R0404
N-Ethylmaleimide	Pierce	Cat# 23030
Iodoacetamide	Sigma	Cat# I1149
TRIzol Reagent	Invitrogen	Cat# 15596018
Leupeptin	ThermoFisher	Cat# 78435
Pepstatin A	ThermoFisher	Cat# 78436
Aprotinin	Sigma	Cat# A6103
Benzamidine	Sigma	Cat# 434760
Phenylmethanesulfonyl fluoride	Sigma	Cat# P7626
cOmplete™, Mini, EDTA-free Protease Inhibitor Cocktail	Roche	Cat# 11836170001
Chloroquine	Sigma	Cat# C6628
MG-132	selleckchem	Cat# S2619
FD Rapid GolgiStain kit	FD NeuroTechnologies	Cat# PK401
Antigen unmasking solution	Vector Lab	Cat# H-3300
DAB substrate Kit	Vector Lab	Cat# SK-4100
Critical commercial assays		
20S Proteasome Assay Kit	Millipore	Cat # APT280
FD Rapid GolgiStain kit	FD Neuro Technologies	Cat # PK401
Deposited data		
RNA-Seq Data	GEO	GSE183383

(*Continued on next page*)

Continued

REAGENT or RESOURCE	SOURCE	IDENTIFIER
Experimental models: Organisms/strains		
Brap knockout mice	generated in house (Lanctot et al., 2013)	https://www.sciencedirect.com/science/article/pii/S1534580713002177
Brap floxed mice	generated in house (Lanctot et al., 2017)	https://www.sciencedirect.com/science/article/pii/S2211124717309713?via%3Dihub
Emx1-Cre mice	JaxMice	Cat# 005628
Thy1-Cre mice	JaxMice	Cat# 006143
Oligonucleotides		
qPCR primers	IDT	See Table S4 for a list of sequences of qRT-PCR primers
Software and algorithms		
Image-Pro Premier	Media Cybernetics	https://www.mediacy.com/support/imagepropremier
Image J	ImageJ	https://imagej.nih.gov/ij/
GraphPad Prism	GraphPad	https://www.graphpad.com/scientific-software/prism/

RESOURCE AVAILABILITY

Lead contact

Further information and requests for resources and reagents should be directed to and will be fulfilled by the lead contact, Yuanyi Feng (yuanyi.feng@usuhs.edu)

Material availability

This study did not generate new unique reagents. All unique/stable reagents used in this study are available from the lead contact with a completed Materials Transfer Agreement.

Data and code availability

RNA-seq data set deposited on GEO: GSE183383. This paper does not report original code. Any additional information required to reanalyze the data reported in this paper is available from the lead contact upon request.

EXPERIMENTAL MODEL AND SUBJECT DETAILS

Mice

Brap knockout (*Brap*$^{-/-}$) and Brap floxed (*Brap*$^{flox/flox}$) mice were generated by conventional mouse embryonic stem cell-based gene targeting (Lanctot et al., 2013, 2017). Brap^{cKONPC} mice were generated by crossing Brap$^{flox/flox}$ mice with the Emx1-Cre mice purchased from JaxMice (stock # 005628). Brap^{cKONeuron} mice were generated by crossing Brap$^{flox/flox}$ mice with Thy1-cre mice purchased from JaxMice (Stock No: 006143). All mice used for this study were housed and bred according to the guidelines approved by the IACUC committees of Northwestern University and Uniformed Services University of Health Services in compliance with the AAALAC's guidelines. Experiments were performed using littermates or age and genetic background matched control and mutant groups in both sexes. Ages of study were from embryonic day 12.5 (E12.5) to one year. For timed matings, the day of vaginal plug was considered E0.5.

Human postmortem cerebral cortical tissue samples

The postmortem brain tissues used in this study were obtained from the University of California Irvine Alzheimer's Disease Research Center (UCI ADRC) and the Institute for Memory Impairments and Neurological Disorders (UCI MIND) through a material transfer agreement. Information on the specimens being analyzed in this study can be found in Table S3: Human Brain Tissue Table.

METHOD DETAILS

Cell culture

Neural stem/progenitor cells were isolated from embryonic cortices at E12.5. Single cells were prepared and cultured in DMEM/F12 with N2 and B27 supplements, Penicillin-Streptomycin, Glutamine, Heparin, and growth factors (20 ng/mL EGF and 10 ng/mL FGF). Mouse embryonic fibroblasts (MEFs) were isolated from embryos at E12.5, after removing head and liver. The embryos were minced and digested in 0.25% trypsin-EDTA at 37°C with agitation for 10 min. Single cell suspensions were plated at a density of $\geq 10^4/cm^2$, which is considered passage 0. The cells were then cultured according to the standard 3T3 cell protocol in DMEM supplemented with 10% FBS and Penicillin-Streptomycin. To block UPS or lysosome, 10 uM MG132, or 25mM chloroquine were applied to MEF culture for 4–12 hours.

Immunoblotting

Immunoblotting of total cell or tissue proteins was performed by extracting with boiling 2x SDS PAGE sample buffer (62.5 mM Tris-HCl, pH 6.8, 2.5% SDS, 0.7135 M β-mercaptoethanol, 10% glycerol, 0.002% Bromophenol Blue) to fully dissolve the tissue proteins, heating at 95°C for 10 min to ensure protein denaturation, and passing through syringes with a $29^{1/2}$ gauge needle three times to sheer nuclear DNA and obtain homogenous extracts. 10–30 ug of total proteins were used for each immunoblotting analysis. Loadings were adjusted and normalized by the total protein content according to Coomassie blue stain of the gel after SDS PAGE and by the level of housekeeping proteins.

Immunostaining, immunofluorescence, and immunohistological analyses

Immunofluorescence staining of cells was carried out by fixing the cells with either 4% formaldehyde or cold methanol, blocking with 1% BSA and 5 mg/ml lysine, and immuno-staining in a buffer containing 25 mM Hepes, pH 7.4, 250 mM Sucrose, 25 mM KCl, 25 mM $Mg(CH_3COO)_2$, 1% BSA, and 0.25% Saponin. For immunofluorescence staining of mouse cortical tissue, mouse brains were fixed by transcardial perfusion with PBS and 4% paraformaldehyde and then processed in 12 um cryosections or 5 um paraffin sections. After treating with antigen unmasking solutions (Vector Labs), brain sections were blocked with 5% goat serum and incubated with primary antibodies in PBS, 0.05% Triton X100, and 5% goat serum at 4°C overnight, and followed by staining with fluorescence conjugated antibodies and Hoechst 33342. Epifluorescence images were acquired with a Leica CTR 5500 fluorescence, DIC, and phase contrast microscope equipped with the Q Imaging Regita 2000R digital camera. For immunohistological (IHC) brain analysis, paraffin sections of 5um thickness were treated with antigen unmasking solutions, blocked with 5% goat serum for one hour, incubated with primary antibodies in PBS, 0.05% Triton X100, and 5% goat serum at 4°C overnight. Then the immunosignals were detected by HRP-conjugated secondary antibodies and the DAB substrate using an ABC kit (Vector lab). IHC images were acquired with a Leica CTR 5500 fluorescence, DIC, and phase contrast microscope equipped a Leica DFC7000 T camera. Images were imported to Adobe Photoshop and adjusted for brightness and black values.

Senescence-associated β-gal (SA-β-gal) staining

For identification of cellular senescence, cells were fixed with 2% formaldehyde and 0.2% glutaraldehyde for 5 min at room temperature. Mouse brains were transcardially perfused and fixed with ice cold PBS followed by 4% paraformaldehyde and 5 mM $MgCl_2$ in PBS for 6–8 hours. The fixed brains were cryopreserved and prepared as cryosections 16 um in thickness. Fixed cells or brain sections were stained with a staining solution containing 5 mM Potassium Ferrocyanide, 5 mM Potassium Ferricyanide, 150 mM NaCl, 5 mM $MgCl_2$, 40 mM Citric acid-Na phosphate buffer pH 5.95, and 1 mg/mL X-gal at 37°C for 6–20 hours.

Golgi-Cox staining and dendritic spine analysis

Mice were euthanized with CO_2; brains were quickly dissected, rinsed with deionized water, immersed in impregnation solution, and processed using FD Rapid GolgiStain kit (FD NeuroTechnologies) according to manufacturer's instructions. Stained sections were examined under a Leica DM5000 light microscope. Pyramidal neurons in the cerebral cortex and hippocampus regions were imaged with a 40x objective and photographed. For dendritic spine density analysis, 16–20 pyramidal neurons in neocortical layer II/III of each mouse were randomly selected for assessment. The number of spines per 10 micrometers in secondary apical dendrites (branched from primary dendrites arising from the soma) was scored using the NIH Image J software.

Histone extractions

Cell or tissues were re-suspended or homogenized and lysed in PBS containing 0.5% Triton X 100, 25 ug/ml leupeptin, 10 ug/ml Pepstatin A, 5 ug/ml Aprotinin, 10 mM Benzamidine, 2 mM PMSF, 10mM *N*-Ethylmaleimide (NEM), 10mM iodoacetamide (IAA), and 0.02% NaN_3 at a density of $\sim 10^7$ cells/ml. Nuclei were first collected by centrifuge at 600 x g for 10 min at 4°C, washed once, and re-suspended in 0.2 N HCl at a density of 4×10^7 nuclei per mL to extract histones overnight at 4°C. After clearing debris by centrifugation at 16,000 x g for 10 min at 4°C, the histone containing supernatants were neutralized with 2 M Tris Base. Protein concentration was determined by measuring absorbance at 280 nm. Histone extractions were stored in aliquots at −20°C.

Cytoplasmic-nuclear fractionation

Cells grown on culture dishes were trypsinized, collected in centrifuge tubes with DMEM and 10% FBS, and washed with PBS. After complete removal of PBS, cells were first treated gently with hypotonic buffer (10 mM Hepes, pH 7.9, 1.5 mM $MgCl_2$, and 10 mM KCl) and protease inhibitors on ice for 10 min before the addition of NP-40 to a final concentration of 0.1%. After gently mixing, cells were spun at 600 x g for 10 min at 4°C. Supernatants were collected and analyzed as cytoplasmic fractions either directly or precipitated by 10% TCA. Pellets were gently washed twice with the hypotonic buffer by spinning at 600 x g for 5 min before being analyzed as nuclear fractions.

RNA isolation and quantitative RT-PCR

Cerebral cortical tissue was homogenized in TRIzol reagent (Thermo Fisher) followed by total RNA extraction according to the manufacturer's protocol. 1ug RNA was reverse transcribed into first-strand cDNA using Superscript III reverse transcriptase (Invitrogen). qRT-PCR reactions were performed using Power SYBR Green PCR Master Mix on a Roche LightCycler 480 Real-Time PCR system. Primers used for accessing gene expression were synthesized according to validated primer sequences from the MGH-PGA PrimerBank, and are listed in Table S4: qRT-PCR primers. Expression was normalized to TATA-binding protein (Tbp) as an internal control and results were analyzed using the $2^{-(\Delta\Delta CT)}$ method.

RNA sequencing analysis of whole cerebral cortical transcriptome

Purified total RNA from whole cerebral cortical tissue of five $Brap^{cKONPC}$ and five control ($Brap^{flox/floxCre-}$ and $Brap^{flox/WTCre-}$) mice at 3 months of age were processed at the University of Chicago Genomics Facility where RNA-seq library preparation was carried out. RNA libraries were sequenced using an Illumina HiSeq 4000 platform (1 × 50 bp single end and/or paired end sequencing). RNA sequencing files were transferred to the Tarbell High-performance computing cluster of Center for Research Informatics at the University of Chicago for analysis. The quality of raw sequencing data was assessed using FastQC v0.11.5. All RNA reads were first mapped to the mouse reference genome (mm10) using STAR v2.5.2b release with default parameters. Picard v2.8.1 (http://broadinstitute.github.io/picard/) was used to collect mapping metrics. The counted reads were filtered to exclude reads with identical library- and molecule barcodes. Differential gene expression analysis was performed using the DESeq2 package. Significance was defined as FDR <0.1 and absolute Fold Change ≥1.5.

10-Plex tandem mass tags (TMT) proteomic analysis

Five $Brap^{cKONPC}$ and five control ($Brap^{flox/floxCre-}$ or $Brap^{flox/WTCre-}$) mice at 6 months of age were transcardially perfused with ice cold PBS and protease inhibitors to remove high-abundant blood and serum proteins. Cerebral cortical tissue was dissected on ice, flash frozen in liquid nitrogen, and sent to the Thermo Fisher Center of Harvard Medical School where the samples were processed for 10-plex TMT analysis. MS2 spectra were searched using the SEQUEST algorithm against a Uniprot composite database derived from Mouse proteome containing its reversed complement and known contaminants. Peptide spectral matches were filtered to a 1% false discovery rate (FDR) using the target-decoy strategy combined with linear discriminant analysis. The proteins were filtered to a <1% FDR. Proteins were quantified only from peptides with a summed SN threshold of >100 and MS2 isolation specificity of 0.5.

Quantified protein were hierarchically clustered using the Euclidean distance, average linkage. Multiple Sample tests (ANOVA) with Permutation-based FDR (FDR <0.05) were performed to see significant changes among two study groups.

20S Proteasome assay

Proteasomes were extracted from mouse cortical tissue in a lysis buffer containing 50 mM HEPES, pH 7.5, 5 mM EDTA, 150 mM NaCl and 1% Triton X-100, 1 uM DTT and 2 mM ATP. Proteasome activities were determined using a 20S proteasome activity assay kit (Millipore APT280) according to manufacturer's instructions. The amount of cleaved AMC fragment of Suc-LLVY-AMC was quantified using a CLARIOstar Plus plate reader (BMG LABTECH) at excitation (EX) = 380/emission (EM) = 460. Reaction mixtures were incubated with 10 μM lactacystin or MG132 before addition of fluorogenic substrates to ensure the specificity of the assays.

QUANTIFICATION AND STATISTICAL ANALYSIS

No statistical methods were used to predetermine sample size, while all experiments were performed with a minimum of three biological replicates and all cell counts were obtained from at least ten random fields. The experiments were not randomized; the investigators were not blinded to the sample allocation and data acquisition during experiments but were blinded in performing quantitative analyses of immunohistological images using the NIH Image J software.

All statistical analyses were done using GraphPad Prism 9.0 software. Data were analyzed by one-way ANOVA or unpaired two-tailed Student's t tests for comparing differences between different genotypes. Differences were considered significant with a p value < 0.05.